Transmural Imaging of Ventricular Action Potentials and Post-Infarction Scars in Swine Hearts

Linwei Wang*, *Member, IEEE*, Fady Dawoud, *Member, IEEE*, Sai-Kit Yeung, *Member, IEEE*, Pengcheng Shi, *Member, IEEE*, KenC. L. Wong, Huafeng Liu, and Albert C. Lardo

***Abstract*—The problem of using surface data to reconstruct transmural electrophysiological (EP) signals is intrinsically ill-posed without a unique solution in its unconstrained form. Incorporating physiological spatiotemporal priors through probabilistic integration of dynamic EP models, we have previously developed a Bayesian approach to transmural electrophysiological imaging (TEPI) using body-surface electrocardiograms. In this study, we generalize TEPI to using electrical signals collected from heart surfaces, and we test its feasibility on two pre-clinical swine models provided through the STACOM 2011 EP simulation Challenge. Since this new application of TEPI does not require whole-body imaging, there may be more immediate potential in EP laboratories where it could utilize catheter mapping data and produce transmural information for therapy guidance. Another focus of this study is to investigate the consistency among three modalities in delineating scar after myocardial infarction: TEPI, electroanatomical voltage mapping (EAVM), and magnetic resonance imaging (MRI). Our preliminary data demonstrate that, compared to the low-voltage scar area in EAVM, the 3-D electrical scar volume detected by TEPI is more consistent with anatomical scar volume delineated in MRI. Furthermore, TEPI could complement anatomical imaging by providing EP functional features related to both scar and healthy tissue.**

***Index Terms*—Bayesian estimation, electroanatomical mapping, inverse problem of electrocardiography, magnetic resonance imaging (MRI), post-infarction scar, transmural electrophysiological imaging.**

I. Introduction

POST-INFARCTION scar tissues, if left untended, can constitute electrophysiological (EP) substrates that could initiate and sustain malignant arrhythmia leading to sudden cardiac death [1]. Characterization of these substrates is critical for defining an effective therapeutic strategy for catheter ablation of ventricular tachycardia (VT) [2]. Current state-of-the-art in VT ablation is guided by electroanatomical voltage mapping (EAVM) during sinus-rhythm [2]. However, point-to-point catheter mapping is still one of the most challenging procedures that incurs prolonged mapping time and exposure to flouroscopy radiation [3]. Furthermore, EAVM provides a poor surface surrogate for deeply-situated scars that often have complex shapes varying with the depth of the myocardium. Therefore, EAVM could result in substantial variability that confounds therapy planning and limits therapy outcome. It may also fail to identify mid-wall fibrosis that is present in up to 30% of patients with nonischemic cardiomyopathy [4]. Recent studies have evidenced the mismatch between EVAM and magnetic resonance imaging (MRI) in characterizing post-infarction scars [2], [3], [5], [6]. Though the cause of this mismatch is still unclear, it is largely believed that EAVM cannot fully detect nontransmural scar core or heterogeneous scar border [6]. Also, poor catheter contact, insufficient chamber sampling and far-field recording in EAVM can lead to false-positives on normal myocardium [2].

This gap in the standard of care calls for a novel imaging modality that could reveal 3-D subject-specific EP characteristics across the depth of the myocardium. This EP imaging modality could also complement traditional tomographic imaging by revealing functional conduction blocks in structurally normal myocardium and by providing electrical functional features related to anatomical scars. It could further compensate for the problem that the routine use of MRI is considered unsafe in the majority of VT patients carrying implantable cardioverter-defibrillators (ICD) [3], [6].

However, the surface-to-volume transition of EP data involves a notoriously ill-posed inverse problem that lacks a unique solution in its most unconstrained case [7]. Starting with body-surface electrocardiograms (ECG), decades of research efforts arrived at surface solutions on the epicardium [8], [9] or the ventricular surface [10], [11]. One of the first successes in surface-to-volume transition examined activation current density, and therefore focused on activation isochrones and initiation sites during electrical depolarization [12].

We have previously developed a novel method of transmural EP imaging (TEPI) that uses body-surface ECG to computationally reconstruct subject-specific, condition-specific *transmural action potentials* [13], [14]. The computed action potentials include not only the depolarization but also the repolarization features, which are closely related to the study of arrhythmia [15] and the location of post-infarction scars. Feasibility of TEPI was

Manuscript received October 14, 2012; revised December 18, 2012; accepted December 20, 2012. Date of publication December 28, 2012; date of current version March 29, 2013. Authorship order reflects relative contributions. This work is supported in part by the RIT GCCIS Seed Funding 2012-2013, RIT GCCIS FEAD Award 2012, SUTD-ZJU Collaboration Research Grant 2012 SUTD-ZJU/RES/03/2012, the National Basic Research Program of China (2010CB732504), the National Natural Science Foundation of China(61271083) and Zhejiang Provincial Natural Science Foundation of China (LR12F03001). *Asterisk indicates corresponding author.*

*L. Wang is with the Computational Biomedicine Laboratory, Golisano College of Computing and Information Sciences, Rochester Institute of Technology, Rochester, NY 14623 USA (e-mail: linwei.wang@rit.edu).

F. Dawoud and A. C. Lardo are with the Johns Hopkins University School of Medicine, Baltimore, MD 21218 USA.

S.-K. Yeung is with Singapore University of Technology and Design, 119878 Singapore.

P. Shi and K. C. L. Wong are with the Computational Biomedicine Laboratory, Golisano College of Computing and Information Sciences, Rochester Institute of Technology, Rochester, NY 14623 USA.

H. Liu is with the State Key Laboratory of Modern Optical Instrumentation, Zhejiang University, Hangzhou 310027, China.

Color versions of one or more of the figures in this paper are available online at http://ieeexplore.ieee.org.

Digital Object Identifier 10.1109/TMI.2012.2236567

preliminarily verified on human subjects with prior myocardial infarction, with reference to **either** *in vivo* EAVM [16] **or** contrast-enhanced MRI [17].

In this study, we generalize TEPI to using heart-surface electrical data as inputs, in particular unipolar electrograms (EGM) available from standard EAVM procedure. The previously studied ECG-TEPI, because of its noninvasive data acquisition, has the potential to facilitate a safer/earlier diagnosis and the continuous monitoring of EP dysfunctions. In comparison, EGM-TEPI uses less smeared data closer to the heart and does not need anatomical data of the torso. It thus sees more immediate potential in EP laboratories to provide transmural details that better guide therapy planning. In this study we test the feasibility of EGM-TEPI on two swine hearts (one healthy and the other with chronic infarction) that were provided through *STACOM 2011 EP simulation challenge* [18].

Another focus of this study is to investigate the relation between TEPI and two other state-of-the-art modalities (EAVM and MRI) for post-infarction scar delineation. We no longer consider a single modality of reference data, but incorporate and compare both EAVM and MRI on each animal. Furthermore, *ex vivo* MRI data are included to further reduce the uncertainty in the reference of 3-D scar shape. Our feasibility study demonstrates the potential of TEPI to complement surface catheter mapping by providing the missing information along the transmural dimension. Our preliminary data also show that, compared to EAVM, TEPI is more consistent with MRI in scar delineation. It indicates that TEPI can also complement tomographic imaging by providing EP functional features around scar tissue or structurally normal myocardium.

II. Forward and Inverse Bioelectrical Problems of the Heart

Various approaches to EP imaging using body-surface ECGs [8]–[12] essentially aim to solve the inverse problem on the bioelectrical field of the heart, where the solution is formulated as different source generators equivalent to the action currents across the depth of the myocardium. Because of the quasi-static property of the bioelectrical field (capacitive, propagation, and inductive effects are negligible) [7], we have previously shown [19] that the potential field within the *volume conductor* can be formulated as

$$\sigma_{blk}\nabla^2\phi_{ext}(\mathbf{r}) = \nabla\cdot(-\mathbf{D}_{\rm int}(\mathbf{r})\nabla u(\mathbf{r})), \quad \forall \mathbf{r}\in\Omega_h \quad (1)$$

$$\sigma_i\nabla^2\phi_i(\mathbf{r}) = 0, \qquad \forall \mathbf{r}\in\Omega_i, \bigcup_i \Omega_i = \Omega_{t/h}. \quad (2)$$

- Equation (1) represents a *Poisson's equation* on the *bidomain heart model*, governing the distribution of extracellular potentials ϕ_{ext} within the 3-D myocardium Ω_h as a result of the current density $\mathbf{J}_{\rm int} = -\mathbf{D}_{\rm int}(\mathbf{r})\nabla u(\mathbf{r})$, where u is the transmembrane potential (action potential). $\mathbf{D}_{\rm int}$ is the anisotropic intracellular conductivity tensor reflecting fiber directions, and σ_{blk} is the bulk conductivity assumed to be isotropic in our formulation [19].
- Equation (2) represents a *Laplace's equation* on the *monodomain torso model*, governing the potential field ϕ in the volume conductor $\Omega_{t/h}$ external to the heart and bounded by the body-surface. The subscript i denotes each piecewise homogeneous region Ω_i with conductivity σ_i, providing a general description of the inhomogeneous volume conductor of the torso.

Boundary conditions of equations (1) and (2) enforce continuous potentials and currents along the normal direction of the bounding surface and any interface Γ_{ij} between regions Ω_i and Ω_j of different conductivities. By Green's theorem and integration by parts, we have shown that the relation between the potential field and cardiac current sources can be derived as follows [7], [19]:

$$\sigma_\xi\phi(\xi) + \int_{\Gamma_o}\sigma[q^*(\xi,\mathbf{r})\phi(\mathbf{r}) - \phi^*(\xi,\mathbf{r})\frac{\partial\phi(\mathbf{r})}{\partial\vec{n}}]\,d\Gamma_o - \sum_{ij}\int_{\Gamma_{ij}}(\sigma_i-\sigma_j)q^*(\xi,\mathbf{r})\phi(\mathbf{r})\,d\Gamma_{ij} = -\int_\Omega \phi^*(\xi,\mathbf{r})[\nabla\cdot(\mathbf{D}_{\rm int}(\mathbf{r})\nabla u(\mathbf{r}))]\,d\Omega, \forall\xi\in\Omega \quad (3)$$

where $\phi^*(\xi,\mathbf{r}) = (1/4\pi|\xi-\mathbf{r}|)$ and $q^*(\xi,\mathbf{r}) = (\partial\phi^*(\xi,\mathbf{r})/\partial\vec{n})$. This (3) provides a general description of the bioelectrical field on a volume conductor Ω, where surface Γ_o is the outer-surface that bounds the volume Ω, and Γ_{ij} are the internal surfaces that divide regions of different conductivities. In other words, (3) tells us that the potential at any point ξ is contributed by two sources: the volume integral of the *primary source* of myocardial current density on the right-hand side (rhs) of (3), and the surface integral of the induced *secondary sources* on all the surfaces expressed in the form of equivalent layer sources. More specifically, it includes the contribution from the bounding surface Γ_o as a consequence of sources that lie outside Ω (second term on the lhs), and the contribution from internal surfaces as an effect of the discontinuity in conductivity (third term on the lhs).

From this general description (3), various existing inverse formulations could be derived. If we restrict our attention to the potential field in the volume excluding the heart, the bounding surface Γ_o now includes the body surface Γ_t and the heart surface Γ_h ($\Omega\equiv\Omega_{t/h}, \Gamma_o\equiv\Gamma_h\cup\Gamma_t$). In this case, the volume integral on the rhs of (3) vanishes and the resulting forward bioelectrical model relates the potential on the heart surface to that on the body surface. Based on this formulation, most existing approaches to the corresponding inverse problem seek the equivalent layer on the heart surface to represent the action sources in the myocardium [8]–[11].

A. Forward Bioelectrical Model for TEPI

In our problem, we target transmural action potentials and include the bidomain heart model in the volume conductor.

1) ECG-TEPI: In our previous study of TEPI, we examined the complete torso and the bounding surface Γ_o was equivalent to the body surface ($\Omega\equiv\Omega_t, \Gamma_o\equiv\Gamma_t$). The heart surface Γ_h was treated as an internal surface that contributed to a part of the summation term on the lhs of (3), i.e., as one of the equivalent layer sources resulting from the inhomogeneity inside and outside the myocardium.

2) EGM-TEPI: To generalize TEPI to inputs from heart-surface EGMs, we now consider only the 3-D bidomain heart

model Ω_h bounded by the heart surface Γ_h ($\Omega \equiv \Omega_h, \Gamma_o \equiv \Gamma_h$). Assuming an isolated heart with no outgoing current flow, we again have a specific form of (3).

For both formulations we showed that, by a coupled *Meshfree* and *Boundary-Element* approach [19], we can numerically solve (3) and convert it to a matrix representation

$$\mathbf{A}\Phi = \mathbf{B}\mathbf{u} \tag{4}$$

where matrix $\mathbf{A}$ is obtained from boundary element method (BEM) approximating the surface integral on the lhs of (3), and matrix $\mathbf{B}$ from the meshfree method approximating the volume integral on the rhs. The vector $\mathbf{u}$ represents the transmural action potential distribution, defined as macroscopic quantities to represent collective behavior over small volumes of tissue. In ECG-TEPI, the vector Φ is the potential field on all the surfaces including the body surface. In EGM-TEPI, Φ consists of only heart-surface potentials. The use of macroscopic scale is determined by the fact that the data Φ available for the inverse problem are at the organ level.

B. Ill-Posedness of the Inverse Problem

To understand the ill-posedness of the inverse problem in calculating transmural action potential $\mathbf{u}$ from different surface potentials Φ (body-surface versus heart-surface), we first obtain the forward transfer matrix through a minimum norm solution to (4): $\Phi = \mathbf{H}\mathbf{u}$. The resulting $\mathbf{H}$ is an $m \times n$ matrix ($m < n$) where n is the number of discrete points in the heart model, and m is the number of data points on the surface. Applying *singular value decomposition* on the forward transfer matrix $\mathbf{H}$, we have

$$\Phi = \mathbf{H}\mathbf{u} = \tilde{\mathbf{U}}\mathbf{S}\tilde{\mathbf{V}}^T\mathbf{u} = \tilde{\mathbf{U}}\mathbf{S}\mathbf{u}_{\tilde{\mathbf{v}}} \tag{5}$$

where matrices $\tilde{\mathbf{U}}$ and $\tilde{\mathbf{V}}$ consist of columns of the left- and right-singular vectors of $\mathbf{H}$, and the vector $\mathbf{u}_{\tilde{\mathbf{v}}}$ represents an orthogonal transformation of $\mathbf{u}$ to the space spanned by the right-singular vectors $\tilde{\mathbf{V}}$. $\mathbf{S}$ is an $m \times n$ matrix composed of an $m \times m$ diagonal matrix of the singular values of $\mathbf{H}$. The remaining $n - m$ columns of $\mathbf{S}$ are all 0-valued.

First, regardless of the spectrum of the singular values, the last $n - m$ elements of $\mathbf{u}_{\tilde{\mathbf{v}}}$ do not contribute to Φ. In other words, the *observable* components in $\mathbf{u}$ are those mapped into the subspace spanned by the first m right singular vectors of $\mathbf{H}$. The rest are *silent*. Theoretically, given data Φ at one time instant, there exists no way to assess those *silent* components. This provides us with a high-level understanding of the limited observability of $\mathbf{u}$ given measurement data Φ.

Second, the first m components $u_{\tilde{\mathbf{v}},i}$ ($i = 1 : m$) in the transformed vector $\mathbf{u}_{\tilde{\mathbf{v}}}$ are modulated by their corresponding singular values σ_i^s before contributing to Φ. As the value of σ_i^s decreases, the contribution of $u_{\tilde{\mathbf{v}},i}$ to Φ decreases to the range of noise or below. To estimate these components from Φ will thus be substantially affected by the noise in Φ.

In the following we use $\mathbf{H}_t$ and $\mathbf{H}_h$ to denote the forward transfer matrices for ECG-TEPI and EGM-TEPI, respectively. For ECG-TEPI, we examined $\mathbf{H}_t$ of eight different human anatomical models [16], [17]. For EGM-TEPI, we examined $\mathbf{H}_h$ of the two swine models under study.

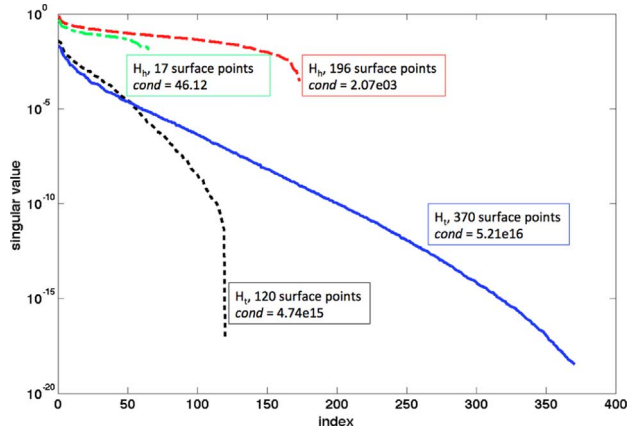

Fig. 1. Singular value spectrum (displayed in a semi-logarithmic plot) of two forward transfer matrices $\mathbf{H}_t$ involved in ECG-TEPI, and another two $\mathbf{H}_h$ involved in EGM-TEPI. $cond$ denotes the condition number of the matrix. Note the different dimensions of m of these matrices (number of data points on the heart/body surface) as labelled in the figure.

- *Decay of singular values:* As illustrated in Fig. 1, singular value spectrums of the eight different $\mathbf{H}_t$ matrices show similar patterns and degrees of decay, and so do the two $\mathbf{H}_h$ matrices. However, matrices $\mathbf{H}_t$ display a drastically faster decay of singular values in comparison to $\mathbf{H}_h$.
- *Condition number* (the ratio between the largest and smallest nonzero singular values): All the eight matrices $\mathbf{H}_t$ have condition numbers at the magnitude from $e + 15$ to $e + 16$ with an average value of $4.06e + 16$, indicating severe ill-posedness of the problem. In contrast, the two matrices $\mathbf{H}_h$ considered in this study have a much smaller condition number of $2.07e + 03$ and 46.12, respectively.

Note that: 1) shape and range of the singular value spectrum of $\mathbf{H}_t$ are similar to those reported in literature [20], where inverse solutions are formulated on the epicardium (condition numbers are at the magnitude of the inverse of double machine precision ϵ^{-1}); and 2) by acquiring measurements closer to the cardiac sources, the ill-conditioning of the problem appears to be reduced in EGM-TEPI. Given the anatomical data derived from tomographic images of any individual subject, the forward biophysical model (4,5) can be created and lays the foundation of the inverse problem [see Fig. 2(a)].

III. Bayesian Maximum a Posteriori Estimation of Transmural Action Potential Dynamics

As the first step towards the generalization of TEPI, we directly apply the same methodology to both ECG- and EGM-TEPI. To resolve the nonuniqueness of the solutions, proper priors and assumptions about the solution must be made. In this regard, we have a unique advantage that physiological knowledge of action potentials are available from decades of research on cardiac physiological modeling [see Fig. 2(b)]. Fig. 2(c) summarizes the two fundamental components of TEPI.

1) Incorporate physiological, spatiotemporal priors of 3-D action potentials through probabilistic treatment of computational models of 3-D electrical propagation.

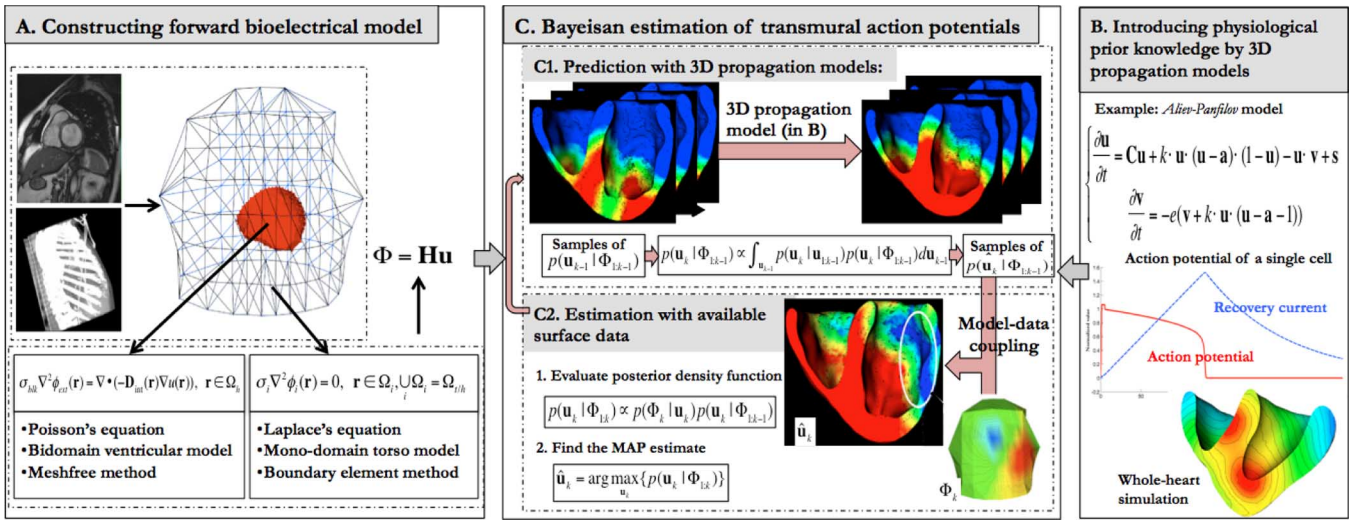

Fig. 2. Summary of the major components in TEPI approach.

2) Combine this probabilistic prior with surface data of uncertainty to obtain a *maximum a posteriori* (MAP) estimate of subject-specific action potentials.

The Bayesian approach is fundamentally a statistical view of regularization. In the statistical setting, we view the transmural action potential $\mathbf{u}$ and the surface potential Φ as random fields. We seek an estimate of $\mathbf{u}_k$ at each time instant k to maximize the posterior density function of $\mathbf{u}_k$ given all the measurements available up to the time instant k, $\Phi_{1:k}$, where $k = 1, \ldots, t_{\max}$ and $t_{\max}$ is the total number of data points of Φ in time

$$\hat{\mathbf{u}}_k = \arg\max_{\mathbf{u}_k} \{p(\mathbf{u}_k|\Phi_{1:k})\}. \tag{6}$$

Although $\mathbf{u}_k$ are time-varying, the quasi-static formulation allows us to proceed as if steady-state conditions existed at any instant [7], and to assume that Φ_k at each time instant is independent with each other. The physiological priors of $\mathbf{u}$ further allow it to be modeled as a Markov process in time (explained later Section III-A1). Combining these assumptions with *Bayes rule*, the posterior distribution $p(\mathbf{u}_k|\Phi_{1:k})$ can be evaluated by a pair of mutually recursive formulations

$$p(\mathbf{u}_k|\Phi_{1:k-1}) \propto \int_{\mathbf{u}_{k-1}} p(\mathbf{u}_k|\mathbf{u}_{k-1}) \underline{p(\mathbf{u}_{k-1}|\Phi_{1:k-1})} d\mathbf{u}_{k-1} \tag{7}$$

$$p(\mathbf{u}_k|\Phi_{1:k}) \propto p(\Phi_k|\mathbf{u}_k) \underline{p(\mathbf{u}_k|\Phi_{1:k-1})}. \tag{8}$$

- Prediction with 3-D propagation models (Fig. 2 C1): (7) first makes a prediction of the distribution of $\mathbf{u}_k$ in the absence of data Φ_k. This prior density function is calculated as an integral over the complete statistical space of $\mathbf{u}_{k-1}$, involving the known posterior density function $p(\mathbf{u}_{k-1}|\Phi_{1:k-1})$ and the probabilistic prior knowledge of $\mathbf{u}_k$ conditioned on $\mathbf{u}_{k-1}$.
- Estimation with available data (Fig. 2 C2): (8) then incorporates the likelihood function $p(\Phi_k|\mathbf{u}_k)$ that captures the dependency of the data Φ_k on the random field $\mathbf{u}_k$. Therefore, the posterior density function $p(\mathbf{u}_k|\Phi_{1:k})$ combines the priors together with the measurement data. The MAP estimate generated in (6) then provides a rational estimate of $\mathbf{u}_k$ that balances its conformity with the prior and its fidelity to the data.

A. Prediction: Physiological Spatiotemporal Priors

We propose that physiological knowledge of the spatiotemporal evolution of action potentials can be embedded as a *blackbox* process behind (7). As illustrated in Fig. 2 C1, we achieve this by incorporating a computational model of 3-D electrical propagation, $\mathbf{u}_k = g(\mathbf{u}_{k-1})$, and the integral involved in (7) is approximated by Monte-Carlo (MC) simulation and integration of $g(\mathbf{u}_{k-1})$ over the space of the posterior distribution of $\mathbf{u}_{k-1}$.

1) A Priori EP Model [Fig. 2(b)]: To describe the *a priori* spatiotemporal process of action potentials, $\mathbf{u}_k = g(\mathbf{u}_{k-1})$ is currently chosen to be the discrete version of the monodomain two-variable *Aliev-Panfilov* model [21]

$$\begin{cases} \frac{\partial \mathbf{u}}{\partial t} = \mathbf{C}\mathbf{u} + \mathbf{k} \cdot \mathbf{u} \cdot (\mathbf{u} - \mathbf{a}) \cdot (\mathbf{1} - \mathbf{u}) - \mathbf{u} \cdot \mathbf{v} + \mathbf{s} \\ \frac{\partial \mathbf{v}}{\partial t} = -\mathbf{e} \cdot (\mathbf{v} + \mathbf{k} \cdot \mathbf{u} \cdot (\mathbf{u} - \mathbf{a} - \mathbf{1})) \end{cases} \tag{9}$$

where $\mathbf{v}$ represents the recovery current, and $\mathbf{s}$ the time-varying stimuli vector that contains information of the location, duration and amplitude of the applied external stimuli in the ventricles. The matrix $\mathbf{C}$ relies on the 3-D myocardial structure and its conductive anisotropy, and vectors $\mathbf{e}$, $\mathbf{k}$ and $\mathbf{a}$ consist of transmural parameters that determine action potential properties at different regions of the heart.

Per the definition of prior knowledge, values of all the relevant model parameters are adopted *a priori*from [21] and thus not subject specific. External stimuli for the earliest ventricular excitation are selected from the four ventricular sub-endocardial regions as experimentally determined in [22]. Because the *Aliev-Panfilov* model (9) is dimensionless with $u \in [0, 1]$ and $t \in [0, 150]$, the amplitude and duration of the stimuli are set to be 1.0 and 1.7 (reflecting a 5 ms duration of the stimuli in a physiologically meaningful 450 ms ventricular EP cycle). Although not subject-specific, this setup of $\mathbf{s}$ provides a reasonable *a priori* knowledge (with uncertainty) of the Purkinjie end-terminals that are hardly available in subject-specific data.

The model uncertainty is reflected by a noise term ω in the discrete version of (9)

$$\mathbf{u}_k = g(\mathbf{u}_{k-1}) + \omega \tag{10}$$

where the explicit form of $g(\mathbf{u}_{k-1})$ depends on the numerical methods used for differentiating $\partial\mathbf{u}/\partial t$. In current study, the implicit fourth-order Runge-Kutta method [23] is used. Note that, because $\mathbf{v}$ is not directly related to the measurement data Φ, we treat it as an intermediate variable in model (10).

The Markov assumption of $\mathbf{u}$ is now justified by $g(\mathbf{u}_{k-1})$: because the derivative of $\mathbf{u}$ with respect to time t in (9) is not higher than the first-order, it is reasonable to obtain a discrete (10) where $\mathbf{u}_k$ depends only on $\mathbf{u}_{k-1}$.

2) EP-Model Based Evaluation of Priors (Fig. 2C1): Unlike most Bayesian applications where the prior takes a static form or goes through a linear transition, the prior $p(\mathbf{u}_k|\Phi_{1:k-1})$ here is dynamic and needs to be evaluated through (7). Since the conditional prior knowledge $p(\mathbf{u}_k|\mathbf{u}_{k-1})$ does not have an explicit form but is described by the nonlinear EP model (10), the integral in (7) can not be evaluated analytically. Instead, it needs to be approximated by MC simulation and integration of the EP model $g(\mathbf{u}_{k-1})$ over the posterior distribution of $\mathbf{u}_{k-1}$. To achieve this, first we draw a set of l samples $\{\mathcal{U}_{k-1,i}\}_{i=1}^{l}$ of $\mathbf{u}_{k-1}$ from the posterior density function of $\mathbf{u}_{k-1}$. On the individual samples, we run the probabilistic EP model (10) to generate a corresponding set of samples $\{\mathcal{U}_{k,i}\}_{i=1}^{l}$ to approximate the mean and covariance of $p(\mathbf{u}_k|\Phi_{1:k-1})$ as follows:

$$\mathbf{u}_k^- = \sum_{i=1}^{l} w_i^m \mathcal{U}_{k,i} \tag{11}$$

$$\mathbf{P}_{\mathbf{u}_k}^- = \sum_{i=1}^{l} w_i^c (\mathcal{U}_{k,i} - \mathbf{u}_k^-)(\mathcal{U}_{k,i} - \mathbf{u}_k^-)^T + \mathbf{Q}_\omega \tag{12}$$

where w_i^m and w_i^c are the weights associated with each sample. $\mathbf{Q}_\omega$ is the covariance matrix of model noise ω. To further improve efficiency, we use a *quasi*-MC method that, known as the *Unscented Transform* [24], replaces the computationally-expensive random sampling with a deterministic sampling scheme that generates a *minimal* set of samples to approximate the posterior density function of $p(\mathbf{u}_{k-1}|\Phi_{1:k-1})$ up to the second-order moment (covariance).

Though the *Aliev-Panfilov* model (9) is a relatively simple, macroscopic model compared to other biophysical EP models, it is selected to serve its role as a blackbox process to implicitly describe $p(\mathbf{u}_k|\mathbf{u}_{k-1})$ in (7). As described above, this means a probabilistic treatment of the EP model involving MC simulation over the complete space of $\mathbf{u}_{k-1}$. Considering the complexity of this procedure (7), the *Aliev-Panfilov* model (9) is a suitable choice: it captures the macroscopic phenomenon of our targeted solutions (action potentials), without introducing any computation that is not feasible during the MC-integration in (7) or unidentifiable scales/variables in the MAP estimate (6). The use of cellular models is subject to the scrutiny of its computational feasibility and identifiability, even though theoretically (7) provides a general setting to incorporate arbitrary types of EP models as a blackbox. This will be reserved for future investigation.

B. Estimation-Minimum Mean Square Error Estimate

1) Evaluation of Posterior Density Function and its MAP Estimate (Fig. 2C2): After we obtain the prior $p(\mathbf{u}_k|\boldsymbol{\phi}_{1:k-1})$ from (7), the posterior distribution $p(\mathbf{u}_k|\boldsymbol{\phi}_{1:k})$ can be updated according to the Bayes rule in (8). The MAP estimate can then be generated as the solution to the optimization problem in (6). Due to the high dimensionality of the random field $\mathbf{u}_k$, we take advantage of the widely-used Gaussian statistics so that the probabilistic density functions involved in equations (7) and (8) can be completely described by their mean and covariance matrices, and the posterior density function (8) can be evaluated analytically. Furthermore, the MAP estimate of a Gaussian distribution exactly coincides with its mean.

After the *quasi*-MC integration (7), (11) and (12) as explained earlier, the Gaussian prior can be represented as

$$p(\mathbf{u}_k|\boldsymbol{\phi}_{1:k-1}) \sim \mathcal{N}(\mathbf{u}_k^-, \mathbf{P}_{u_k}^-). \tag{13}$$

Because of the linearity of the measurement model (4)

$$\Phi_k = \mathbf{H}\mathbf{u}_k + \nu, \quad \nu \sim \mathcal{N}(\mathbf{0}, \mathbf{R}_\nu) \tag{14}$$

where Φ and measurement uncertainty ν are also Gaussian, $p(\boldsymbol{\phi}_k|\mathbf{u}_k)$ also follows a Gaussian distribution:

$$p(\boldsymbol{\phi}_k|\mathbf{u}_k) \sim \mathcal{N}(\mathbf{H}\mathbf{u}_k, \mathbf{R}_\nu). \tag{15}$$

Combining Gaussian distributions (13) and (15), the posterior density function $p(\mathbf{u}_k|\boldsymbol{\phi}_{1:k})$ in (8) can be analytically calculated as $p(\mathbf{u}_k|\boldsymbol{\phi}_{1:k}) \sim \mathcal{N}(\hat{\mathbf{u}}_k, \hat{\mathbf{P}}_k)$, where [25]

$$\begin{aligned} \hat{\mathbf{u}}_k &= \mathbf{u}_k^- + \mathbf{K}_k(\Phi_k - \mathbf{H}\mathbf{u}_k^-), \quad \hat{\mathbf{P}}_k = (\mathbf{I} - \mathbf{K}_k\mathbf{H})\mathbf{P}_{\mathbf{u}_k}^- \\ \mathbf{K}_k &= \mathbf{P}_{\mathbf{u}_k}^- \mathbf{H}^T (\mathbf{H}\mathbf{P}_{\mathbf{u}_k}^- \mathbf{H}^T + \mathbf{R}_\nu)^{-1}. \end{aligned} \tag{16}$$

The MAP estimate (mode) of this Gaussian posterior density function equals its mean $\hat{\mathbf{u}}_k$, at which the density function takes its maximum value. The above solution (16) is equivalent to the general linear minimum mean square error (MMSE) estimate used in the Kalman filter (KF), where $\mathbf{K}_k$ is obtained by minimizing the trace of the posterior covariance matrix $\hat{\mathbf{P}}_k$.

2) Connection With Tikhonov Regularization: To better understand the regularization nature of the Bayesian approach, we rewrite the objective function (6) according to the monotonicity properties of the logarithm

$$\hat{\mathbf{u}}_k \propto \arg\max_{\mathbf{u}_k} \{\ln p(\mathbf{u}_k|\boldsymbol{\phi}_{1:k-1}) + \ln p(\boldsymbol{\phi}_k|\mathbf{u}_k)\}. \tag{17}$$

Because of the Gaussian distributions (13) and (15), we have

$$\ln p(\mathbf{u}_k|\boldsymbol{\phi}_{1:k-1}) \sim -\frac{1}{2}||\mathbf{u}_k - \mathbf{u}_k^-||^2_{(\mathbf{P}_{u_k}^-)^{-1}} \tag{18}$$

$$\ln p(\boldsymbol{\phi}_k|\mathbf{u}_k) \sim -\frac{1}{2}\|\Phi_k - \mathbf{H}\mathbf{u}_k\|^2_{\mathbf{R}_\nu^{-1}}. \tag{19}$$

Equation (17) becomes equivalent to

$$\hat{\mathbf{u}}_k = \arg\min_{\mathbf{u}_k} \{\|\Phi_k - \mathbf{H}\mathbf{u}_k\|^2_{\mathbf{R}_\nu^{-1}} + \|\mathbf{u}_k - \mathbf{u}_k^-\|^2_{(\mathbf{P}_{u_k}^-)^{-1}}\}. \tag{20}$$

Therefore, in the Gaussian case, the MAP estimation (20) can be interpreted as Tikhonov regularization with the following particular choices.

- First, *weighting matrices* that correspond to the covariance matrices of the data and the priors. Therefore, rather than heuristic adjustment of a regularization parameter λ, the relevant importance of data and priors are controlled by natural and rational parameters of physical interpretations, i.e., covariance matrices that represent their uncertainties. This facilitates the incorporation of multiple complex constraints. Also, in addition to a point estimate, this approach gives as a by-product the posterior covariance matrix $\hat{\mathbf{P}}_k$ to measure the uncertainty of the solution.
- Second (more important to TEPI), *physiological priors* $\mathcal{N}(\mathbf{u}_k^-, \mathbf{P}_{u_k}^-)$ that are described by probabilistic treatment of a dynamic EP model. The sequential Bayesian setting is able to accommodate such priors. In comparison, it would be difficult to incorporate this complex prior in deterministic regularization. For example, the commonly used Tikhonov regularization term $\lambda\|\mathbf{L}\mathbf{u}_k\|^2$ is equivalent to the simplest assumption of prior density functions: $p(\mathbf{L}\mathbf{u}_k) \sim \mathcal{N}(\mathbf{0}, \lambda^{-1}\mathbf{I}_n)$, i.e., $\mathbf{L}\mathbf{u}_k$ is assumed to be spatially uncorrelated and of equal variance, where $\mathbf{L}$ is the weight matrix and λ controls the regularization level.

Algorithm Summary and Implementation Details

In summary, TEPI builds on a sequential Bayesian estimator realized through a recursive procedure of the following.

1) Prediction of the prior $p(\mathbf{u}_k|\Phi_{1:k-1})$ in the absence of data Φ_k (7), through *quasi*-MC simulation and integration of the *Alive-Panfilov* model over the space of $\hat{\mathbf{u}}_{k-1}$.
2) Evaluation of the posterior density function $p(\mathbf{u}_k|\Phi_{1:k})$ to further incorporate the dependency of Φ_k on $\mathbf{u}_k$ (8), done analytically by (16) because of the Gaussianity.
3) Eventually, generation of the point estimate that maximizes the value of the posterior density function (6). In the case of Gaussian, this MAP estimate coincides with the mean of the posterior density function.

Fig. 2 provides a summary of the major components in TEPI.

3) Prior Assumptions: An initial prior of $p(\mathbf{u}_0)$ is needed to start the sequential estimator. Because $\mathbf{u}_0$ represents the resting action potential field, in current study we assume $p(\mathbf{u}_0)$ to be a zero-mean Gaussian distribution $\sim N(\mathbf{0}, \mathbf{P}_{\mathbf{u}_0})$. Since prior knowledge of stimuli location is incorporated through the vector $\mathbf{s}$ in the EP model (9), we desire small uncertainty about the resting status of $\mathbf{u}_0$. Therefore, the covariance matrix $\mathbf{P}_{\mathbf{u}_0}$ is set to be $1e\text{-}4\mathbf{I}_n$ for very small probability of nonzero values. This prior starts the Bayesian estimator by $p(\mathbf{u}_1|\boldsymbol{\phi}_1) \propto p(\boldsymbol{\phi}_1|\mathbf{u}_1)\int_{\mathbf{u}_0}[p(\mathbf{u}_1|\mathbf{u}_0)p(\mathbf{u}_0)]\,d\mathbf{u}_0$ as described in (6) and (8), and this sequential procedure repeats until the end of the input ECG or EGM time series $t_{\max}$.

Other prior knowledge includes the covariance matrices for Gaussian noises ω and ν. In our study, we assume that the covariances of ω and ν have the simplest possible structures

$$\omega \sim \mathcal{N}(\mathbf{0}, \mathbf{Q}_\omega), \mathbf{Q}_\omega \equiv \sigma_\omega^2 \mathbf{I}_n$$
$$\nu \sim \mathcal{N}(\mathbf{0}, \mathbf{R}_\nu), \mathbf{R}_\nu \equiv diag(\sigma_\nu^2)$$

where the model noise ω is spatially uncorrelated and of equal variance among all the nodes in the heart. σ_ω^2 is set to be $1e-3$, resembling a 30 dB signal-to-noise ratio (SNR) given an average signal energy of $[0, 1]$-valued $\mathbf{u}$. We also assume that the measurement noise ω is uncorrelated between each pair of the electrodes. The variance at each electrode is derived assuming 20 dB SNR on the corresponding spatial location of the input signals $\Phi_{1:t_{\max}}$. Fig. 18 (Appendix) provides a list of all the notations and symbols used in this paper, including the different assumptions of parameters in the *Aliev-Panfilov* model and hyperparameters of the statistics.

4) Computational Cost: TEPI is computationally intensive, because the generation of priors (7) involves *quasi*-MC simulation of the *Aliev-Panfilvo* model, and the calculation of posterior density functions (16) involves large-matrix operations. For example, on a ventricular model with $2000+$ discrete nodes (typical dimension used in TEPI), though the *Aliev-Panfilov* model takes merely ~ 2 min to complete the simulation of one ventricular EP cycle on a Macintosh desktop (3 GHz Intel Xeon), predicting the prior by (7) involves ~ 4000 model-simulations that raise the computation time to $100+$ h. The subsequent evaluation of posterior density function by (8) involves large-matrix operations at $\mathcal{O}(n^3)$ and, as observed in our previous experiments, involves a similar amount of computational time as the prediction phase. Thus the complete procedure of TEPI typically requires about 250 h for input ECG or EGM data of one QRST cycle. Most recently, we began investigating the potential of graphic processing units (GPU) in accelerating TEPI. Our first effort reported a promising $16\times$ speedup of TEPI on a Tesla C2070 GPU card [26]. Combined with a more recent CPU system (Intel i5), TEPI computation using GPU can be reduced to the range of 2 (Tesla cards) to 4 (GTX card) hours [26].

5) Classification of Post-Infarction Scar: To detect conduction blocks and post-infarction scars from the MAP estimate $\hat{\mathbf{u}}_{1:t_{\max}}$, we examine its depolarization (action time AT) and repolarization (action potential duration APD) features. First, we examine ventricular AT pattern by 26×3 local regions, with 17 LV divisions by AHA standards [27], 9 RV divisions in a similar manner [28], and three transmural layers in each division. On each segment, we calculate the average difference in activation time (dAT) between the MAP estimates $\hat{\mathbf{u}}_{1:t_{\max}}$ and the simulated healthy $\mathbf{u}_{1:t_{\max}}^{sh}$ assuming sinus-rhythm excitation. K-means clustering is then applied on dAT to classify all the 78 segments into three groups: *normal, premature*, and *delayed* excitation. This will give us an initial knowledge of the conduction blocks in the ventricles. Second, we further incorporate the repolarization feature APD because it is closely related to the occurrence of myocardial scar. In particular, we calculate the averaged change in AT (dAT) and APD (dAPD) extracted from $(\hat{\mathbf{u}}_{1:t_{\max}} - \mathbf{u}_{1:t_{\max}}^{sh})$, and then apply k-means on this feature $(dAT + dAPD/2)$ among all the ventricular nodes to differentiate them into two groups: *healthy* and *scar*. It is important to notice that AT and APD are *functional* parameters, thus the detected scars are electrically rather than anatomically defined.

IV. Experiments and Results

A. Validation Study Design and Experimental Data Processing

Evaluations of EGM-TEPI are performed on data acquired on two preclinical swine models, one healthy and the other with

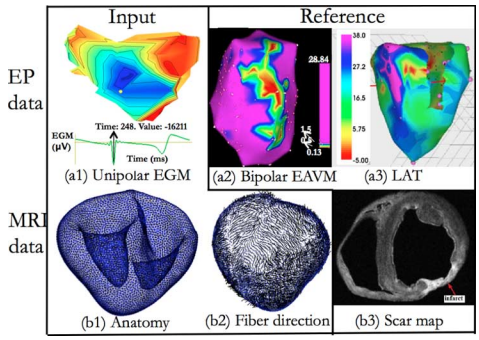

Fig. 3. Experimental data from *in vivo* EP mapping and *ex vivo* MRI study. TEPI input data include time sequences of CARTO unipolar EGM (a1), and anatomical data (b1) derived from un-weighted MRI with 3-D fiber directions (b2) from DW-MRI. Reference data include CARTO activation times (a3, color bar in ms), and for the infarcted heart CARTO bipolar EAVM (a2, color bar in mV) and 3-D anatomical scar from DW-MRI (b3). Figures (a2) and (b3) are provided by the STACOM'11-EP simulation challenge website.

five-week old chronic infarct, collected by researchers at the Sunnybrook Research Institute (Toronto, ON, Canada) and provided to the participants in the *STACOM 2011 EP simulation Challenge* [18]. For both swine models, *in vivo* electroanatomical mapping and *ex vivo* MRI data were provided. In the following we describe the specific setup of our validation study. For details of the animal models or data acquisition, please refer to [18].

1) In Vivo EP Mapping Data: In addition to the coordinates of the mapping points, the following *in vivo* endocardial and epicardial EP data (CARTO-XP system, Biosense Webster, Inc., Diamond Bar, CA, USA) are used for the purposes of our study.

- *Input data:* EGM. In the current study we consider epicardial unipolar EGMs as inputs to the proposed EGM-TEPI. In theory, this could be generalized to endocardial and/or epicardial EGMs, and will be investigated in future study. In order to temporally align EGM signals that were recorded over several beats, we examine the range of heart rhythm observed in the EGM data. Because the EP data were recorded in stable sinus rhythm, the ranges of cycle lengths collected are relatively stable at 777–820 ms (77–73 bpm, healthy) and 620–640 ms (96–93 bpm, infarct) excluding occasional beats of preventricular complexes (PVC). Therefore, temporal alignment of these EGM signals is done by the best matching QRS complexes in body surface lead III. Electrograms with correlation $\geq 90\%$ are selected as input signals. Fig. 3(a1) shows a snapshot of the temporally aligned epicardial EGM map on the healthy swine heart.
- *Reference data:* EAVM scar and activation isochrones. From CARTO bipolar voltage maps [Fig. 3(a2)], scar area on the infarcted swine heart is delineated using clinical cutoff threshold <1.5 mV. It consists of dense scar core and scar border. Epicardial and endocardial activation times, as illustrated in Fig. 3(a3), have outliers removed before being used as reference isochrone maps.

2) Ex Vivo MR Imaging Data: MRI data obtained *ex vivo* (1.5T GE SignaExcite) are used in the following manner.

- *Input data:* anatomy and fiber direction. High-resolution 3-D anatomical mesh [extracted from the unweighted MR images as shown in Fig. 3(b1)] and fiber structure [estimated from DW-MR images as shown in Fig. 3(b2)] were provided to this study by researchers at Siemens Corporate Research (Princeton, NJ, USA) and INRIA, Asclepios project (Sophia Antitpolis, France). For TEPI, meshfree, macroscopic representations of the same ventricles are generated with spatial resolution of ~ 2000 nodes. This is required for the algorithmic feasibility of TEPI to target the *identifiable* scale given macroscopic surface EGM data with limited spatial resolution of ~ 10-10^2 data points, and for the computational feasibility of TEPI to perform high-dimensional probabilistic estimation.
- *Reference data: anatomical scar.* On the infarcted heart, reference data of the 3-D volume of scar tissue delineated from DW-MR images is provided by researchers at Sunnybrook Research Institute (Toronto, ON, Canada). It was previously shown that, using DW-MRI on *ex vivo* formalin-fixed swine hearts, the regions of increased apparent diffusion coefficient (ADC) correlated very well with dense scars [29]. Fig. 3(b3) shows a selected short-axis DW-MR image where infarct areas are observable with elevated image signal intensity.

3) Registration of Carto and MRI Data: Because CARTO mapping and MR imaging were performed separately, proper registration is needed to establish physical correspondence between the two sets of data. Due to the lack of landmarks that could specify their pair-wise correspondence, we resort to the two best available data sources for registration.

- Epicardial and endocardial scar areas on CARTO surface (areas S_c with low voltage) and on MR-derived surface (areas S_i with elevated image signals). We define the *consistency* between two scar areas as the percentage of overlaps $(S_c \bigcap S_i)$ in the total areas $(S_c \bigcup S_i)$. Nevertheless, because the mismatch of EAVM and MRI scar data has been observed and reported extensively [2], [3], [5], [6], [30], it is incorrect to assume a hard constraint of *perfect match* of scar areas to guide the registration. Also this information is not available on the healthy heart.
- General anatomical shapes of the ventricles recorded in both CARTO and MRI data. Due to the lack of known correspondence in landmarks, we consider the average distance from all the CARTO points to the MRI-derived surface. This shape-based registration is generally valid. However, it is also error-prone because CARTO mapping has relatively low resolution, and there is often a large discrepancy between anatomical shapes derived from CARTO and those derived from MRI.
- The problem is further complicated by the different heart shape and size *in vivo* and *ex vivo*. In addition, the above two criteria of registration appear to be in conflict as observed in the infarcted model under study.

Following a typical clinical procedure, we perform an initial rigid registration (rotation + translation) through visual inspection by an expert. It is performed in the commercial software platform Amira (Visualization Sciences Group, Burlington, MA, USA), which allows 1) visual inspection of ventricular shapes, anatomical landmarks and scar areas, 2) manual selection of corresponding regions from CARTO and MRI data, and

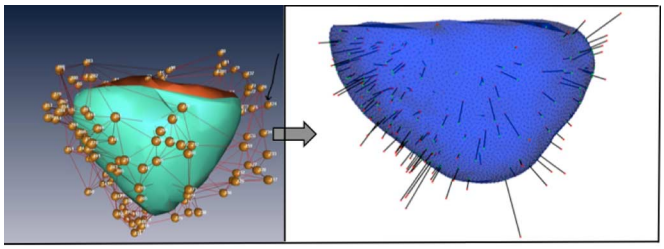

(a) (b)

		Healthy Heart	Infarcted Heart
Distance (mm)	Epi	4.58 ± 3.23	5.25 ± 3.99
	LV-Endo	6.90 ± 3.62	3.65 ± 2.87
Scar consistency	Epi	N/A	21.25%
	LV-Endo	N/A	25.29%

(c)

Fig. 4. Illustration of the registration procedure. (a) Initial rigid registration. Orange points and wired-mesh represent epicardial CARTO points. (b) Perpendicular projection of CARTO points (red) to the MRI-surface, initialized by (a). Projected points are colored green. (c) Registration errors representing matching of anatomical shapes and scar areas, respectively.

3) export of the final transformation matrix. While carrying out this process on the infarcted heart, we observe that the attempt to maximize the scar overlap would deteriorate the match of anatomical shapes, and vice versa. To resolve this conflict, we choose an outcome that balances the two registration criteria. This process is illustrated in Fig. 4(a). To refine the initial registration, we establish the correspondence by the nearest-distance (perpendicular) projection of CARTO points to MRI-derived surface as illustrated in Fig. 4(b). The two measures on the match of anatomical shapes and scar areas are summarized in Fig. 4(c).

B. Results

In the following experimental validation, we focus on the following.

- The quantitative accuracy of TEPI in computing the activation pattern (on both hearts), which may reveal abnormal conduction behavior unseen in structural imaging.
- The quantitative accuracy of TEPI in localizing post-infarction scar (on the infarcted heart), which will reveal its relation with the state-of-the-art EAVM and MRI.

For experiments on each animal model, we consider two cycles of TEPI. The first cycles of TEPI are performed assuming *a priori* knowledge listed in Fig. 18, i.e., 1) healthy uniform model parameters and regular Purkinje end-terminals to initialize the *Aliev-Panfilov* model (9), and 2) Gaussian priors with predefined covariances. According to TEPI outcomes of the first cycles, we update the locations of the initial ventricular activation sites (see Section V-A) to initialize the second cycles of TEPI with all the other assumptions remaining the same.

1) Healthy Heart: Fig. 5 shows the activation isochrone maps measured by CARTO-XP system on the healthy porcine heart. Ventricular excitation appears to start at septal-apical region of LV endocardium (endocardial map) and anterior-middle region of RV (epicardial map), smoothly propagates through anterior walls, and arrives at inferior-lateral LV at last. Because there is a lack of early breakthrough at LV-anterior wall and the LV is activated relatively late compared to RV, the early activation at middle-anterior LV endocardium is probably caused by breakthroughs from the RV anterior excitation. Though measured on a healthy heart, this RV-to-LV activation pattern is different from general human sinus-rhythm excitation. This could be caused either by the difference in Purkinje conduction systems of human and swine hearts, or by certain peculiar conditions of the specific swine heart under study. The aim of TEPI is to reconstruct this pattern of transmural action potentials without knowing the specific locations of electrical stimuli *a priori*.

After temporal alignment of CARTO unipolar EGMs and the registration process, 173 out of 250 CARTO points are selected to provide input EGM signals to TEPI, to reconstruct action potential signals on 1738 meshfree nodes that represent the 3-D ventricular model of the swine.

2) Transmural Action Potentials: Fig. 6(a) shows snapshots of *Aliev-Panfilov* simulation with prior knowledge listed in Fig. 18, i.e., the physiological spatiotemporal prior for TEPI if assimilation of observation data does not occur. As expected, both ventricles are activated simultaneously, with a slight earlier total activation of LV than RV. Fig. 6(b) shows corresponding snapshots of transmural action potentials computed by TEPI under this prior, exhibiting a RV-to-LV activation where RV is excited earlier than LV and the latest activation occurs in inferior-lateral LV wall. This agrees with CARTO mapping data, particularly in terms of the *unusual* activation pattern specific to this heart, i.e., the apex-to-base, RV-to-LV activation, an early activation at middle-lower anterior LV possibly caused by breakthroughs from other stimuli, and the latest endocardial activation at inferior wall of the LV. Fig. 7(a) shows the action potential duration (APD) computed by TEPI. As expected, this healthy heart has a smooth and uniform distribution of APD throughout the myocardium. Because the prior assumption of Purkinje terminals on the septal region of RV may be incorrect, we hypothesize that it may lead to an incorrect estimation of early activation at that region and thus a long APD as shown in the results.

3) Activation Isochrones Versus CARTO Data: Fig. 7 (b.3) shows the anterior view of the computed epicardial activation isochrone and error maps, versus CARTO data (b.1) and the simulated sinus-rhythm prior (b.2). As shown, the prior (b) used to constrain TEPI shows LV-to-RV epicardial activation opposite to that measured by CARTO (a). In comparison, TEPI outcome shows early RV activation and RV-to-LV, anterior-to-inferior propagation. Nevertheless, the initial assumption of an anterior LV stimulus is not completely corrected. Similarly, Fig. 8 shows the anterior-lateral view of the computed LV-endocardial activation isochrone and error maps. Again, because of the assumption of Purkinje end-terminals, the prior (b) shows a base-to-apex activation that is opposite to CARTO data (a). Despite this false prior, TEPI manages to capture the relatively earlier activation at middle-anterior LV endocardium and the subsequent apex-to-base activation.

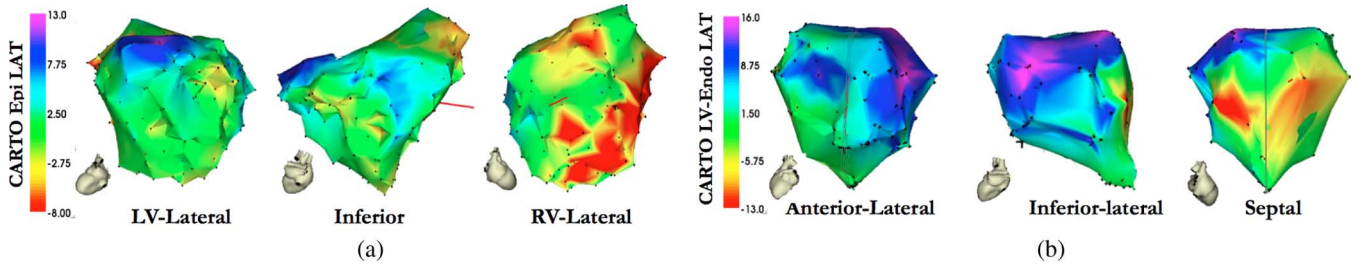

Fig. 5. Activation isochrone maps acquired by CARTO system on the healthy swine heart. Color bar encodes the activation time (ms).

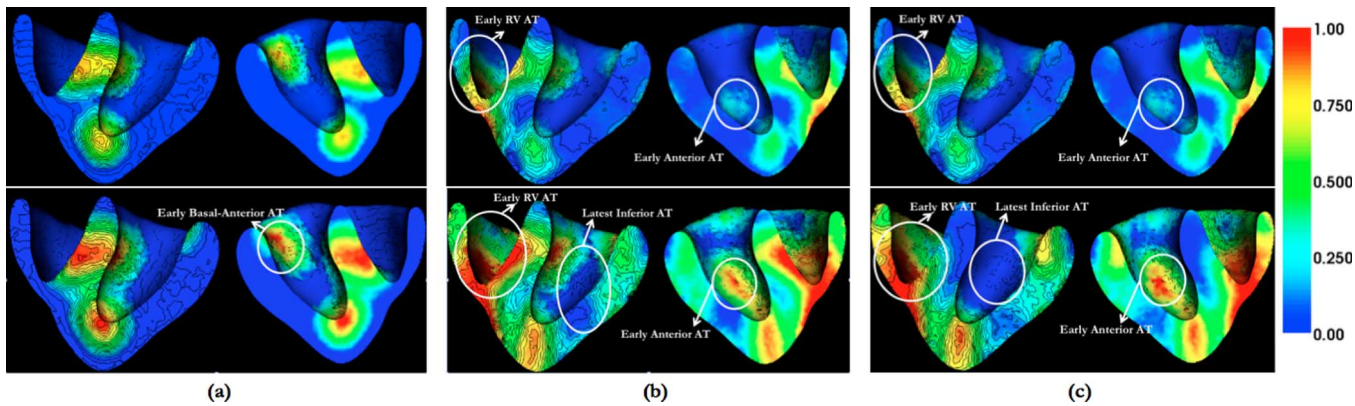

Fig. 6. Transmural action potentials (encoded by color bar, dimensionless) at 14 and 24 ms after the onset of ventricular excitation on the healthy swine.

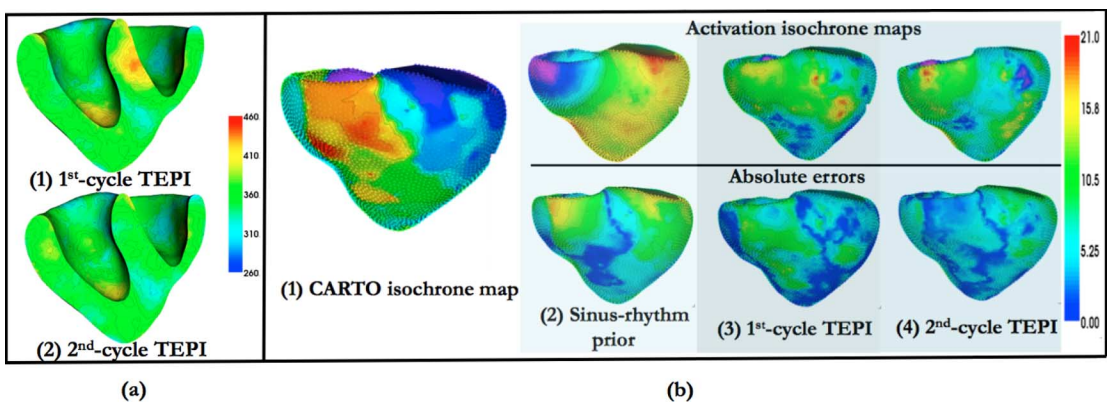

Fig. 7. (a) Transmural action potential durations (encoded by color bar in ms) computed by TEPI. (b) Epicardial activation isochrone and error maps (encoded by color bar in ms) between TEPI estimations and CARTO measurements.

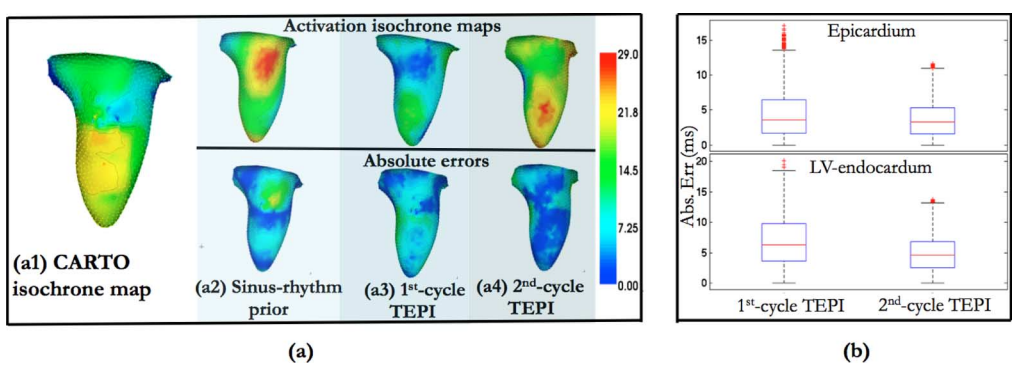

Fig. 8. (a) Endocardial activation isochrone and error maps (encoded by color bar in ms) between TEPI estimations and CARTO measurements. (b) Box plots of the absolute errors of the computed activation time. The center, lower bound and upper bound of the box represents the median (50%, lower quartile (25%) and higher quartile (75%) of the data. The lower and higher bound of the whisker represent the minimum and maximum of the data that lie within the 1.5 IQR (interquartile range) below and above the lower and higher quartile of the data, respectively. The red points above the whisker represent outliers.

Fig. 9 lists the *absolute errors* and *correlation coefficients* between the computed and the measured isochrones. Fig. 8(b) shows boxplots of the absolute errors of the computed activation time on all the epicardial and endocardial nodes. As shown, the

Healthy (total activation time)	Absolute error (median ± std, ms)			Correlation coefficient		
	Cycle 1	Cycle 2	Reduction	Cycle 1	Cycle 2	Increase
Epi (21ms)	3.58±3.29	3.32±2.47	7.32%	0.4088	0.7482	1.83
LV-Endo (29ms)	6.32±4.29	4.70±3.07	25.61%	0.4566	0.7765	1.70

Fig. 9. Absolute errors and correlation coefficients between the computed and CARTO-measured activation time.

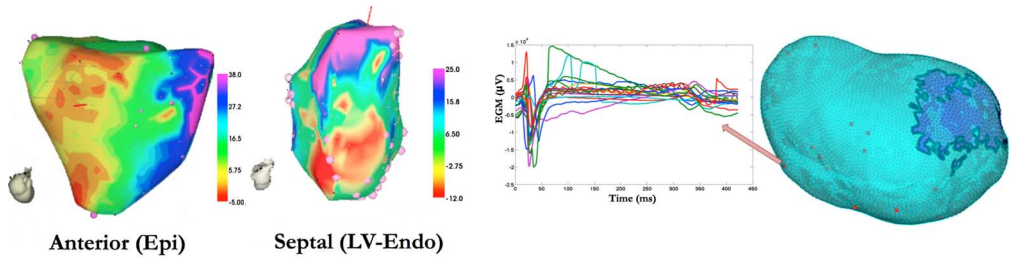

Fig. 10. (a) Examples of activation maps measured by CARTO-XP systems on the infarcted swine heart. Color bar encodes the activation time (ms). (b) Locations (red points) and temporal traces of the input EGM signals, shown on the epicardial surface of the MRI-derived anatomical model. Epicardial scar area as detected in MRI data is highlighted blue.

majority ($\sim 75\%$, upper bound of the box) of the computed activation time has relatively low absolute errors that are below the median $+\ 0.6745$ std (standard deviation) of the error distribution, i.e., 75% of the estimation has absolute error ≤ 5.80 ms on the epicardium and ≤ 9.22 ms on the LV endocardium. A small portion of the estimation shows larger absolute errors (the upper portion of the whisker), including a few *outliers* (red points above the upper bound of the whisker) that has an absolute error beyond the 1.5 interquartile range (IQR) above the 75% of the data ($\geq$ median$+2.698$ std). These regions with large errors are likely to correspond to locations where false prior assumptions of Purkinje end-terminals are not successfully corrected by TEPI, and have contributed to a higher mean and std in the computed absolute errors. The correlation between the computed and measured isochrones are calculated with these outliers removed.

4) Comparison Between Two Cycles of TEPI With Different Assumptions of Initial Activation Sites: Results of the second cycles of TEPI are listed in Figs. 6–9 for snapshots of transmural action potentials, epicardial and endocardial isochrones, quantitative errors of the isochrones and the boxplots of their absolute errors, respectively. As shown, the change of initial activation sites has a visually evident impact on the early phase of endocardial activation, bringing it closer to CARTO data. The rest of the activation has relatively less prominent changes, and appears to *converge* to similar features to those of the first cycle. Quantitatively, the update of the initial activation sites only moderately improve the median absolute errors of the computed isochrones (Fig. 9, 7.32% and 25.61% reduction of median error for the epicardium and endocardium, respectively). However, it is evident from the boxplots [Fig. 8(b)] that the regions with larger absolute errors are substantially reduced, resulting in a much smaller number of outliers as well as a much narrower whisker that is shifted downwards (smaller error) in the boxplots. This improvement of accuracy is more notable in the increase of the spatial correlation between the computed and measured isochrones: correlations of the second-cycle outcomes are 1.83 (epicardium) and 1.70 times (LV-endocardium) higher than that of the first-cycle.

5) Infarcted Heart: The diseased swine heart under study has a transmural anatomical scar that is centered at middle inferolateral LV, and extends longitudinally and circumferentially to the adjacent areas with decreasing percentage and transmurality [Fig. 3(b3)]. This scar causes substantial delay and/or absence of activation around inferolateral region of LV, as shown in CARTO activation maps [Fig. 10(a)]. CARTO maps also exhibit a RV-to-LV, apex-to-base activation pattern that resembles left bundle branch block (LBBB). The aim of TEPI is to detect the scar and LBBB pattern without any prior knowledge of these specific conditions.

From CARTO data mapped with a six-pole catheter (one tip and six ring electrodes), at current stage we are only able to extract the tip EGM from each of the seven electrodes. After data clean-up, temporal alignment of EGM signals and registration procedure, we are left with 17 CARTO points of unipolar EGMs as the input to TEPI, to reconstruct action potentials on 2084 nodes of the 3-D ventricular myocardium. Locations and traces of these EGM signals are illustrated in Fig. 10(b). Note the lack of CARTO sampling in scar regions.

6) Transmural Action Potentials: Fig. 11(a) shows the transmural depolarization process simulated assuming sinus-rhythm prior knowledge listed in Fig. 18. Under this general prior, Fig. 11(b) shows the transmural action potentials computed by TEPI, where LV excitations are suppressed and RV excitations are advanced, giving an LBBB-like pattern with sequential RV-to-LV, apex-to-base activation that is not normally present in sinus-rhythm ventricular activation. Furthermore, there is a substantial delay at inferior-lateral LV, consistent with the location of the anatomical scar shown in MRI. Fig. 12(a) shows the APD map computed by TEPI. Unlike the healthy heart, there is a larger dispersion of APD on the infarcted heart and a much shorter APD on inferior-lateral LV.

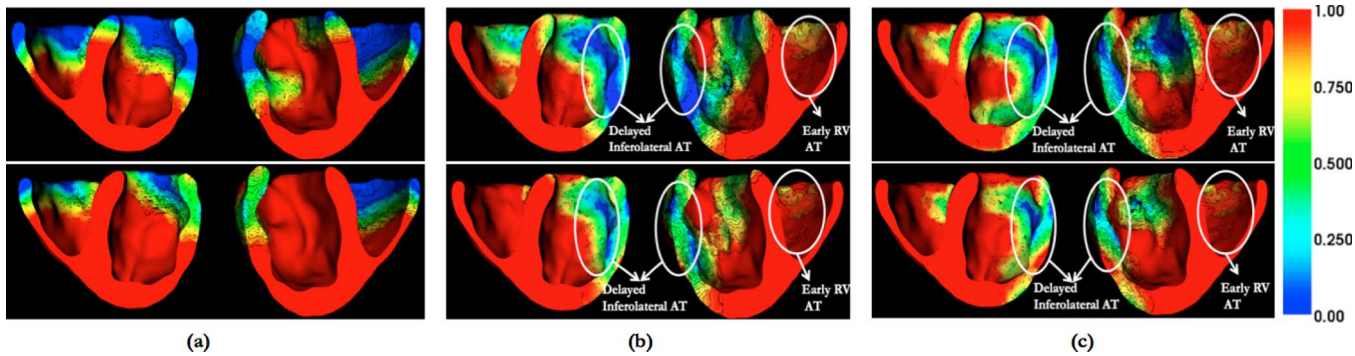

Fig. 11. Transmural action potentials (encoded by color bar, dimensionless) at 34 ms (upper row) and 44 ms (lower row) after the onset of ventricular excitation on the infarcted heart.

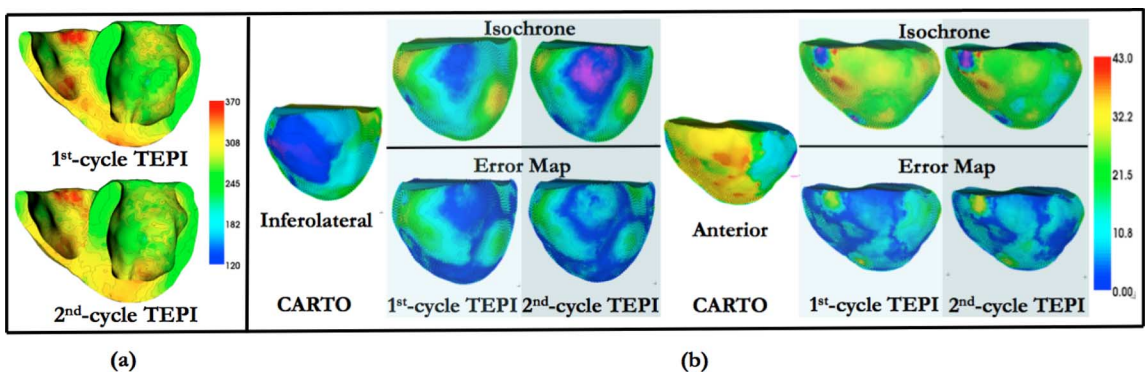

Fig. 12. (a) Transmural action potential durations (encoded by color bar in ms) computed by TEPI. (b) Epicardial activation isochrone and error maps (encoded by color bar in ms) between TEPI estimations and CARTO measurements.

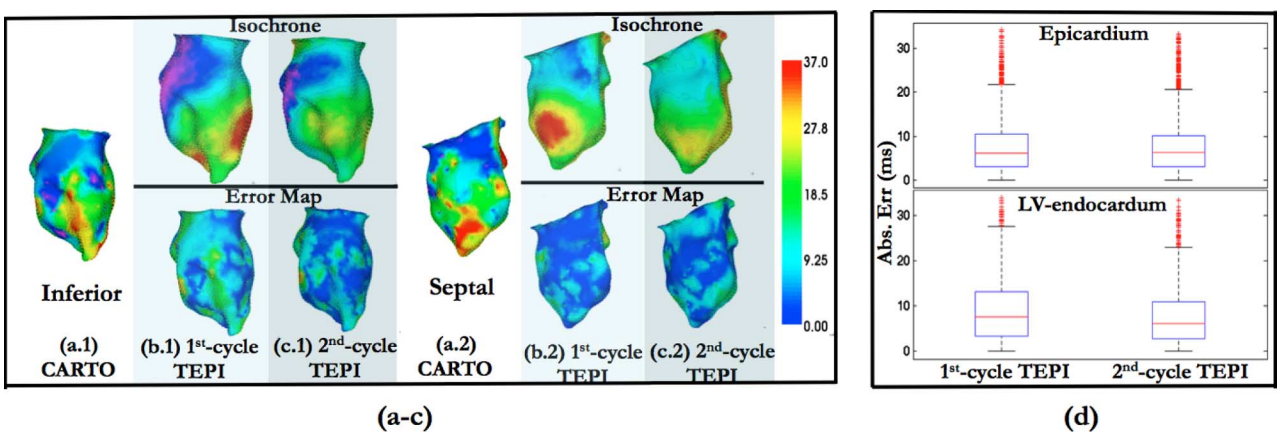

Fig. 13. (a-c) Endocardial activation isochrone and error maps (encoded by color bar in ms) between TEPI estimations and CARTO measurements. (d) Box plots of the absolute errors of the computed activation time, represented in similar forms as those in Fig. 8.

7) Activation Isochrones Versus CARTO Data: Fig. 12(b) and Fig. 13(a)–(c) illustrate multiple epicardial and LV-endocardial views of the computed activation-isochrone and error maps in comparison with CARTO data. The computed epicardial isochrones capture the early RV activation and RV-to-LV propagation pattern through anterior wall, with a substantial late activation at inferolateral wall of LV. The error at anterior-LV is possibly caused by the false initial stimuli assigned to basal-anterior LV endocardium according to [22]. The error at lateral-LV is more difficult to analyze, due to the lack of CARTO data in regions with scar. Similarly, the computed isochrones of LV endocardium capture the apex-to-base activation on the septal wall, the septum to lateral wall propagation and the latest activation at inferolateral LV.

Fig. 14 lists the absolute errors and correlation coefficients of the computed isochrones compared to the CARTO measurements, and Fig. 13(d) shows the boxplots of the absolute errors. Note that this infarcted heart has a longer total activation time compared to the healthy heart, hence the higher absolute error. Similar to what is observed in the healthy heart, about 75% of the computed isochrones (as included below the upper bound of the box) has absolute errors below 9.93 ms (epicardium) and

Infarcted (total activation time)	Absolute error (mean ± std, ms)			Correlation coefficient		
	Cycle 1	Cycle 2	Reduction	Cycle 1	Cycle 2	Increase
Epi (43 ms)	6.13±5.63	6.21±5.57	-1.29%	0.7598	0.7599	1.0
LV-Endo (37ms)	6.54±6.53	6.22±5.71	4.89%	0.4200	0.7239	1.72

Fig. 14. Absolute errors and correlation coefficients between the computed and CARTO-measured activation time.

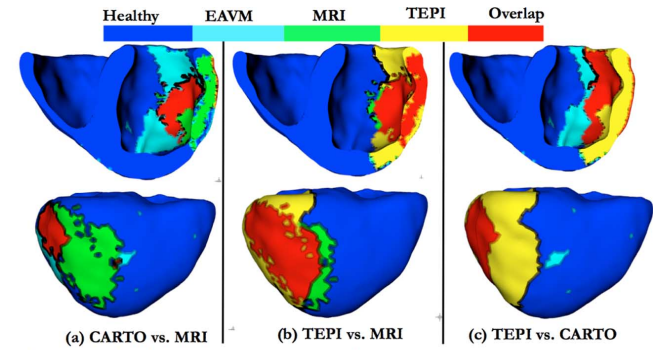

Fig. 15. Superimposed scars localized by CARTO-EAVM (light blue), MRI (green), and TEPI (yellow). Overlap of scars between each of the two methods is highlighted red. Top row: transmural view of inferolateral endocardium. Bottom row: Inferolateral view of epicardium.

11.97 ms (LV endocardium). A small percent of the computed isochrones has larger errors, but the number of outliers is higher than that obtained in the healthy heart. The correlations between the computed and measured isochrones are calculated with these outliers removed.

8) Comparison Between Two Cycles of TEPI: Results of the second cycles of TEPI are listed in Figs. 11–14. Similar change of TEPI outcomes as that seen in the healthy heart can be observed. The change of initial activation sites has a more notable effect on the estimation of endocardial activation, especially by reducing errors caused by the false assumptions on the initial activation locations. This is reflected in the examples of endocardial isochrones in Fig. 13(a)–(c), as well as in the downward shiftting of the box and whisker in the boxplots in Fig. 13(d). Quantitatively, it results in a slight reduction (4.89%) of the median absolute error, and a more evident increase (1.72 times) of spatial correlation between the CARTO data (Fig. 14). The accuracy of epicardial isochrones is notably high in the outcomes of the first-cycle TEPI (a median absolute error $= 6.13$ ms, and correlation coefficient $= 0.76$), and it has a minimal change in the second-cycle. It appears that TEPI is able to capture major disruptions to the electrical propagation path and the performance is not much affected by the assumption on the initial activation sites.

9) Scar Consistency: TEPI, EAVM, and MRI: Fig. 15 illustrates the *consistency* between scars localized from the three modalitiess: CARTO-EAVM (light blue), MRI (green), and TEPI (yellow). Scar *consistency* as defined earlier $(S_1 \cap S_2)/(S_1 \cup S_2)$ is also listed. Notable in Fig. 15(a) is the evident mismatch of the scars detected by CARTO and MRI. Foremost, due to the absence of transmural CARTO data, the overlap only occurs on heart surfaces. On the inferolateral endocardium, CARTO-EAVM shows scar towards the basal and apical areas that is not confirmed in MRI data $(consistency = 25.29\%)$. On the inferolateral epicardium, MRI-delineated scar extends substantially further into inferior epicardium (consistency $= 21.15\%$). This is likely due to the limit of EAVM in detecting nontransmural scar or scar border zone.

Fig. 15(b) and (c) shows the TEPI-detected scar superimposed with MRI and EAVM scars, respectively. On the endocardium, similar to CARTO scar, TEPI scar extends further towards base and apex than MRI scar. Its *consistency* with EAVM substrate (29.71%) or MRI scar (48.58%) on the endocardium is higher than that between EAVM and MRI. On the epicardium, TEPI scar is very similar to MRI scar, covering inferior region that is absent in EAVM data. Its *consistency* with EAVM (28.96%) or MRI scar (64.65%) on the epicardium is also higher than that between EAVM and MRI. Thus, in comparison with EAVM, TEPI is more consistent with MRI in scar delineation.

10) Scar Transmurality: MRI and TEPI: Furthermore, transmural data is available in TEPI and co-localizes well with MRI scar, identifying 85% of the anatomical scar (sensitivity $= 82\%$; specificity $= 84\%$). To further understand the relation between the two transmural scar volumes (electrically defined by TEPI versus structurally defined by MR), we present a *refined* bull's eye representation of scar volume. It is based on the original 17-segment bull's eye representation, and we consider a three-layer transmural division within each segment. As shown in Fig. 16, color bar encodes the scar percentage within each transmural layer in each segment. The total percentage of scar in each segment is labeled on the figure. Out of the eight segments to which the MRI scar extends (segments 11, 5, 10, 6, 16, 15, 12, 4 with decreasing percentage of scar within), TEPI scar occupies the same eight segments with the same center (segment 11), and two adjacent segments with small percentages [13 (15%); 7 (10%)].

For the center of scar mass where the majority of the segment is structurally damaged (93% of segment 11; 51% of segment 5), TEPI scar co-localizes with the anatomical scar with good accuracy (segment 11: 100%, segment 5: 99%). On these two segments, we further calculate the following.

- *Relative size:* The portion of scar in this specific location versus the entire scar volume.
- *Transmurality:* Tthe percentage of three transmural layers in the scar

As summarized in Table I, the majority of the scar is distributed in the epicardial and middle layer, with decreasing percentage transmurally from epicardial to endocardial layer. TEPI and MRI data are consistent in quantifying scar transmurality, particularly in segment 11 that resides in the middle of the scar mass and most likely corresponds to scar core.

For the rest of the structural scar that occupies a moderate percentage of the segment (10%–40%) and is likely to involve outer borders of the scar, the correlation between the anatomical scar and EP scar becomes more intricate and less well understood [30]. This might also explain the small-percentage extension of TEPI scar to two adjacent segments relative to anatomical scar.

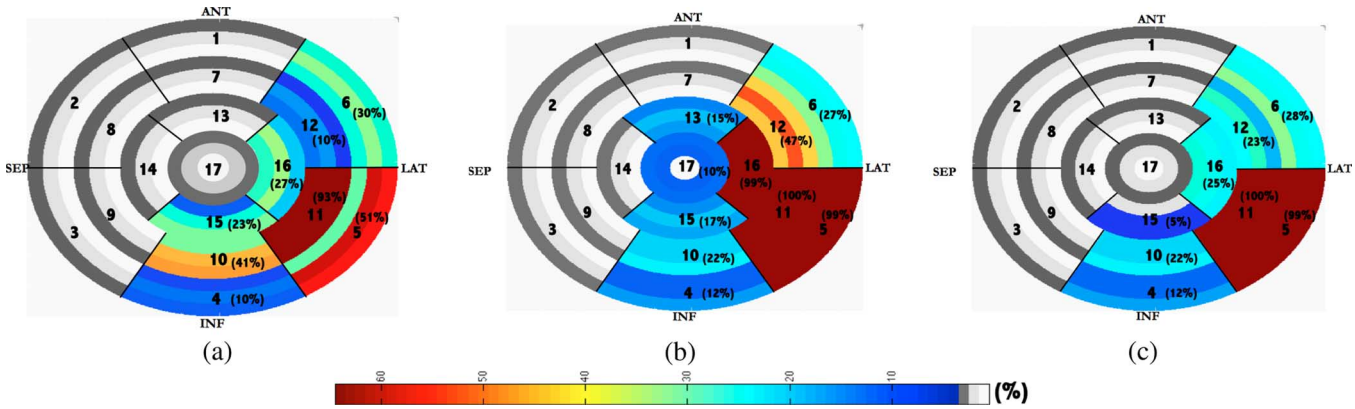

Fig. 16. The *refined* Bull's eye representation of the 17 × 3 segments of LV and the detected scar. (a) MRI anatomical scar. (b) TEPI scar assuming sinus-rhythm prior. (c) TEPI scar assuming LBBB prior as determined from (b). The gray levels within each segment represent the three transmural layers. The color encodes the percentage of scar within each transmural layer. The total percentage of scar in each *infarcted* segment is given on the figures.

TABLE I
RELATIVE SIZE AND TRANSMURALITY OF THE SCAR CORE. THE RELATIVE SIZE EQUALS (THE PORTION OF THE SCAR IN A SPECIFIC SEGMENT)/(THE TOTAL SIZE OF THE SCAR). TRANSMURALITY EQUALS (THE PORTION OF THE SCAR IN EACH TRANSMURAL LAYER)/(THE TOTAL SIZE OF THE SCAR WITHIN THE SEGMENT)

Segment		Size	Epi	Mid	Endo
11	MRI	23.99%	37.92%	31.82%	30.26%
	TEPI	23.94%	38.41%	29.83%	31.76%
	Difference	0.05%	0.49%	1.99%	1.50%
5	MRI	16.42%	42.50%	39.47%	18.03%
	TEPI	18.61%	37.95%	32.72%	29.33%
	Difference	1.19%	4.55%	6.75%	11.30%

Because the arrhythmogenic mechanism of scar border has significant clinical interest and is not yet well understood, the capacity of TEPI in localizing scar core and border will be a major focus of our future study.

Results of scar localization from the second-cycle TEPI is shown in Fig. 16(c), which displays moderate improvement of localization accuracy. TEPI scar of this cycle does not extend to the extra segments 17 and 13 as that of the previous cycle. Quantitatively, the center of EP scar is in good agreement with the scar core (segments 11 and 5) while the percentage of scar segment 16 is reduced from 99% in the first cycle to 25%, much more consistent with the MRI scar.

V. CONCLUSION AND DISCUSSION

In summary, a novel and effective modality of transmural EP imaging is in great demand to address the gap in current clinical practice of EP mapping. However, the transition from surface to volume EP data is a notoriously ill-posed problem that does not have a unique solution in its general unconstrained form. This paper builds on our previously developed solution to this problem, and the main contributions include the following.

1) The generalization of TEPI to inputs from heart-surface EP mapping data. This opens a more immediate clinical potential of TEPI in guiding ablation therapy.
2) The investigation of the consistency among three different modalities (TEPI, EAVM, and MRI) for the delineation of post-infarction scars.
3) The rigorous validation of TEPI involving multiple state-of-the-art *in vivo* and *ex vivo* reference data.

Our feasibility study demonstrates that, with *a priori* assumption from literature, EGM-TEPI is able to capture subject-specific transmural EP pattern with reasonable accuracy, and to localize post-infarction scars across the depth of the myocardium. Furthermore, compared to the low-voltage EAVM scar area, the scar volume detected by TEPI is more consistent with anatomical scar defined by MRI. Both preliminary findings are promising and entail long-term studies.

First, though ECG- and EGM-TEPI are theoretically built on the same physical principles (4) applied to two different volume conductors, practically this change of measurement data may play an important role in the ill-posedness of the problem. As observed in our analysis of $\mathbf{H}$ in Section II-B), the decay and range of the singular value spectrum seem to be similar between ECG-TEPI and other ECG-based inverse formulations but with equivalent source models assumed on the heart surfaces. This indicates that inverse problem formulated on transmural sources may not necessarily be more ill-posed than formulations based on surface equivalent layer sources. Rather it is the nonuniqueness of the solution that calls for special constraints. Second, when the measurement surface is on the heart surface, the inverse problem of EGM-TEPI appears to deal with a much smaller condition number and slower decay of singular values in the forward matrix. This further motivates the new research direction of EGM-TEPI. Future research should investigate the relation and difference between TEPI outcomes in these two applications (as well as potential algorithm revisions in one application or the other).

Furthermore, the application of EGM-TEPI is currently built on an biophysical model assuming an isolated heart with no outgoing current flow. This assumption is proper in the current study because of the open-chest experimental settings (see Section V-B). However, it may not hold in general clinical setting dealing with closed-chest scenarios. Therefore, future investigations need to study the effect of this assumption on an intact heart. We may also extend TEPI to consider the potential application of ECG-EGM-TEPI, the investigation of which require simultaneous body-surface ECG recordings and epicardial EGM recordings.

Second, we observe that anatomical scar and TEPI scar appear to co-localize with good quantitative accuracy at scar

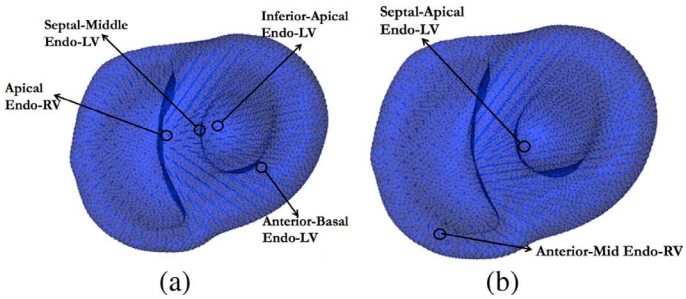

Fig. 17. Stimuli settings for two different cycles of TEPI on the healthy heart. (a) Sinus-rhythm based on general Purkinjie end-terminals determined by [22]. (b) Updated stimuli according to the outcome of TEPI initialized by (a).

core, while displaying a more intricate relation at scar outer border. Similar observations between anatomical scar and recorded EGMs have been reported previously on an electro-mechanical analysis of infarct border zone [30]. In the future, larger experimental studies have to be performed to confirm our preliminary data and, in particular, to examine the relation between anatomical and electrical scar.

Built on essentially the same methodology that was previously validated in our studies of ECG-TEPI [14], [16], [17], this study further demonstrates the feasibility of surface-to-volume transition in the inverse cardiac bioelectrical problem. In the following, we discuss the relevant implications, limitations and future work to follow this study.

A. Physiological Priors and Probabilistic Approach

The Bayesian approach has started to gain popularity in bioelectrical applications [9], [31], [32]. In addition to its ability to accommodate multiple priors of physical interpretation (through covariance matrices), the Bayesian context also provides an opportunity to incorporate a new type of constraints that have not been much used in the inverse bioelectrical problems: dynamic spatiotemporal priors provided by computational models of electrical propagation.

There are two sets of prior assumptions involved in TEPI: those in the EP model and those in the Gaussian statistics.

1) Physiological Priors: Unlike commonly used constraints of spatial/temporal smoothness, physiological prior considers the anisotropic reaction-diffusion process incorporated through stimuli $\mathbf{s}$ and parameters in the EP model (9).

Ventricular Stimuli: The comparison study performed between the two cycles of TEPI provides a good understanding of the impact of the assumption of Purkinje end-terminals on TEPI. The second cycle of TEPI is performed with initial activation sites determined from the outcome of the first cycle of TEPI, whose initial activation sites are located according to the regular locations of Purkinje end-terminals experimentally determined in human hearts [22]. For example, on the healthy swine model, the clustering analysis on AT shows that the activation is suppressed in all the segments with the assumed Purkinje end-terminals. Instead, the earliest premature activation is detected at the endocardial layer of anterior-middle RV (segment 22) and LV apex (segment 17). Based on this, we randomly select a stimulus in each of the two segments. Fig. 17 illustrates the stimuli configuration for the sinus-rhythm prior (a) and the updated prior (b).

Similar observations are obtained on both hearts. The change of initial activation sites appears to have a more evident effect on the computed endocardial isochrones, most likely in reducing the errors in locations where the false assumptions of Purkinje end-terminals cannot be corrected in the first cycle. By the time the electrical propagation reaches the epicardium, the assumption of initial activation sites seems to have a minimal effect on TEPI estimation. Therefore, with the general assumption of Purkinje end-terminals listed in Fig. 18, TEPI is able to reveal the prominent subject-specific electrical propagation as shown in both animal models. When such assumption is updated (potentially more correct), the occurrence of larger errors is reduced as shown in the boxplots [Fig. 8(b) and Fig. 13(d)]. As a result, the overall absolute error (median and std) shows a slight reduction, while the spatial correlations with the CARTO measurement are more substantially increased. This improvement of quantitative accuracy also contributes to a more precise delineation of scar volume. If needed, this prior knowledge could be approximated by examining body-surface ECG data or invasive catheter mapping data, or reconstructed from surface data as proposed in [33].

The observed influence of initial activation sites on TEPI is consistent with the fundamental theoretical aspects behind TEPI. Because TEPI is essentially built on a sequential MAP estimator, the assumption of initial activation sites is expected to impact the prior distribution of $\mathbf{u}$ only in the beginning time steps. As the algorithm iterates in time, the effect of such assumption is circumvented by the data-driven estimation and eventually has minimal effect for estimation in the subsequent time steps. As observed in our previous studies, if only initial activation sites are updated between consecutive TEPI cycles, TEPI outcomes typically converge within three or four cycles. Further improvement of the outcome will have to involve the adapting of other parameters or structures of the EP model.

Model Parameters: Compared to the initial activation location, parameters of the *Aliev-Panfilov* model (9) model ($\mathbf{D}$, a, e, and k) are expected to affect every MAP iteration and to have a larger impact on TEPI outputs. To estimate model parameters together with action potentials is a possible solution. Furthermore, parameter estimation will entail a personalized EP model that can be used for predicting patient response to therapy. While personalization of EP models has shown its predictive power in therapy planning [34], it becomes difficult if the available data are limited to surface mapping data as in this study, e.g., without incorporating *a priori* any data of post-infarction scars. This requires extensive future studies.

2) Bayesian Approach: At current stage, we use several assumptions to simplify the problem that is otherwise algorithmically and computationally complex. These assumptions could be relaxed in the future to a more general setting.

Gaussian Assumption: As explained earlier, the widely-used Gaussian statistics lead to a specific case of MAP estimation that allows a simple evaluation of posterior density functions (16) and is equivalent with a quadratic form in Tikhonov regularization. Nevertheless, equations (6)–(8) could in general accommodate different posterior density functions to be evaluated by Bayes rule. While the specific analytic formulations

Notations	Descriptions
Forward biophysical model	
u, $\mathbf{u}$	Action potential & vectors of transmural action potential u on all meshfree nodes
ϕ, Φ	Surface potential & vectors of potential ϕ measured on all surface electrodes
$\sigma_{bk}, \sigma, \mathbf{D}_{int}$	Bulk conductivity, torso conductivity, and intracellular conductivity tensor
$\Omega, \Gamma, \vec{n}$	Volume conductor, its surface, and the outward normal direction of the surface
$\mathbf{A}$	Matrix approximating surface integral in (3) using the boundary element method
$\mathbf{B}$	Matrix approximating volume integral in (3) using the meshfree method
$\mathbf{H}$	Forward transfer matrix that relates $\mathbf{u}$ to Φ
$\tilde{\mathbf{U}}, \mathbf{S}, \tilde{\mathbf{V}}, \mathbf{u}_{\tilde{\mathbf{V}}}$	Singular value decomposition $\mathbf{H} = \tilde{\mathbf{U}}\mathbf{S}\tilde{\mathbf{V}}^T$, $\mathbf{u}_{\tilde{\mathbf{V}}}$ is the orthogonal transformation of $\mathbf{u}$ to the space spanned by the right singular vectors
Bayesian estimation - variables	
$p(\|)$	Conditional density function
$\mathbf{v}$	Vectors of recovery currents on all meshfree nodes
$\mathcal{U}_{k,i}$	The i-th sample of $\mathbf{u}_k$ according to its probability density function
w_i^m, w_i^c	Weight of the i-th sample to calculate the mean and covariance of the density function
$\bar{\mathbf{u}}_k^-, \mathbf{P}_{\mathbf{u}_k}^-$	Mean and covariance matrix for the *a priori* density function of $\mathbf{u}_k$ without Φ_k
$\hat{\mathbf{u}}_k, \hat{\mathbf{P}}_{\mathbf{u}_k}$	Mean and covariance matrix for the *a posteriori* density function of $\mathbf{u}_k$ given Φ_k
$\mathbf{K}_k$	Optimal *Kalman gain* calculated to update the prediction
Bayesian estimation – prior assumptions	
$\mathbf{u}_0$	Initial action potential field, Gaussian distribution ~ $N(\mathbf{0}, 1e-4\mathbf{I}_n)$, n the dimension of $\mathbf{u}$
ω	Model error ~ $N(\mathbf{0}, \mathbf{Q}_\omega), \mathbf{Q}_\omega = 1e-3\mathbf{I}_n$
ν	Measurement error ~ $N(\mathbf{0}, \mathbf{R}_\nu), \mathbf{R}_\nu$ is diagonal assuming 20dB SNR on input Φ
$\mathbf{C}$	Matrix approximating the anisotropic conduction, assuming conductivity 4.00 along fiber direction, 4.00/6.67 across fiber direction [30];
k, a, e	Parameters determining action potential shape, $k = 8.0$, $a = 0.15$, $e = 0.01$ [21]
$\mathbf{s}$	Ventricular stimuli, located at regular human Purkinje end-terminals [22] duration = 1.7, amplitude = 1.0

Fig. 18. Summary of the notations and symbols used in this paper, including all the assumptions and parameter values used in the Bayesian estimation.

(16) no longer apply, many different techniques can be used for this purpose, such as particle-based Monte Carlo Markov Chain (MCMC) method [25].

Hyperparameters: For simplicity, hyperparameters controling the priors (covariance of $\mathbf{u}_0$, ω and ν listed in Fig. 18) are predefined and fixed in our current study. As explained in (12), the covariance $\mathbf{P}_{\bar{\mathbf{u}}_k}^-$ of the priors $p(\mathbf{u}_k|\Phi_{1:k-1})$ is a combination of the effect from the initial assumption of $\mathbf{P}_{\mathbf{u}_0}$, the nonlinear interaction described in the model (10), as well as the additional model noise $\mathbf{Q}_\omega$. Therefore, the assumption of $\mathbf{P}_{\mathbf{u}_0}$ does not play as important a role as the assumption on the EP model or the statistics of ω and ν.

We have previously quantified the impact of the covariances of ω and ν on TEPI solutions [14], and showed that TEPI was able to deliver a reasonable outcome with the current treatment of hyperparameters. In the future, we aim to develop a principled way of quantifying the relative importance of the data and the priors by extending the Bayesian approach to a hierarchical form. For example, if the covariance of ω is expressed as $\lambda\mathbf{I}$, we could estimate not only the posterior conditional density of $\mathbf{u}$ but also the hyperparameter λ. Furthermore, if we have a variety of constraints, we could incorporate them simultaneously without fixing the relative weight of each component. For example, the covariance for the measurement noise ν could be expressed as $\mathbf{R}_\nu = \gamma_1\mathbf{I} + \gamma_2\mathbf{R}_2$. The identity matrix $\mathbf{I}$ represents the independent and uniform noise over the electrodes. Covariance between close or distant electrodes can be introduced in $\mathbf{R}_2$. The relative importance of the different components of noise variances is then balanced through the hyperparameters γ_1 and γ_2. This can be done by an expectation-maximization algorithm where posterior density functions and hyperparameters are estimated recursively. Such a hierarchical Bayesian approach will ultimately replace the heuristic alternatives that predefine hyperparameters.

B. Experimental Data Acquisition and Processing

One of the uncertain factors and challenges of this study lies in the preparation of experimental data.

First, the epicardial catheter mapping was performed in a open-chest fashion. This nonstandard use of CARTO system may produce substantial errors, and the open-chest setting may alter the shape and physiological state of the heart. In an alternative closed-chest fashion, epicardial mapping can be done by entering pericardial space percutaneously and mapping with CARTO system. Second, because CARTO data are acquired through a point-by-point mapping process, beat-to-beat variability and occasional PVC beats require extra care. Because the mapping was performed when the animals were under stable sinus-rhythm, we try to overcome the variability of activation over different beats by rejecting epicardial electrograms from dissimilar lead III beats. This however still introduces uncertainty and largely reduces the number of input data available to TEPI. Third, because of the limited sampling resolution of CARTO and our limited knowledge in extracting unipolar EGMs from the ring electrodes of the six-pole catheter, the number of inputs for TEPI is very small. All the above factors need to be acknowledged during the validation process.

Furthermore, one of the most challenging tasks during the data processing arises in the attempt to spatially register *in vivo* CARTO mapping and *ex vivo* MR imaging data. This is essentially caused by the lack of landmarks that could specify the *absolute* correspondence between the two datasets. Instead we have two plausible criteria, i.e., anatomical shapes and scar locations, which could partially guide the registration but neither could be completely trusted. This problem is further complicated by the fact that these two criteria appear to be in conflict, and that the heart shape may have altered between *in vivo* and *ex vivo* studies. In our study, we considered alternative nonrigid registration methods to overcome the potential limitations of a *rigid registration followed by perpendicular registration* caused by the low dimensionality and initial error of the rigid registration. However, even though higher-dimensional nonrigid transformation may have offered better shape correspondence, the match of scar areas was ignored and led to even lower match between CARTO and MRI scar data. Facing this ill-defined registration problem, we opted for a balanced compromise between the match of anatomical shape and the match of scar area (when available). In order to optimally balance the two criteria, new registration algorithms may need to be developed. This topic is beyond the scope of the current research and will be investigated in future studies.

C. Scientific Versus Diagnostic Capacity

At current stage, TEPI has limited accuracy in precisely quantifying action potential signals (*scientific capacity*) [14], [17]. Yet it suffices to capture the subject-specific abnormal action potential *pattern* (*diagnostic capacity*), which allows us to quantify activation/repolarization isochrone patterns with reasonable accuracy [34], and to detect regions responsible for abnormal EP behavior such as post-infarction scars [17]. Similar observations were made in a recently proposed approach to transmural action potential reconstruction and its application in identifying myocardial ischemia [35].

As shown in (3), cardiac current density is proportional to the spatial gradient of action potential $\nabla\mathbf{u}$. Mathematically, the existence of this gradient operator ∇ on the rhs of (3) decides that there are different quantitative values of $\mathbf{u}$ that would give the same potential field in the torso. To give a trivial but concrete example, given a specific vector $\mathbf{u}$ and a constant vector $\mathbf{c}$, $\nabla\mathbf{u} \equiv \nabla(\mathbf{u}+\mathbf{c})$ because ∇ of a constant field is zero. Therefore, without any prior constraint, the solution to (4) could be any $\mathbf{x}$ as long as it satisfies $\nabla\mathbf{x} = \nabla\mathbf{u}_r$, $\mathbf{u}_r$ being the *true* solution of action potentials. This lays one of the theoretical causes of the pattern-wise accuracy of the reconstructed action potentials. This also explains the necessity of *physiological* priors to reduce the solution space.

The gradient operator ∇ in (3) also relates to another detail of TEPI implementation regarding the dimensionless value of $\mathbf{u} \in [0, 1]$ in the *Aliev-Panfilov* model. Commonly, an empirical conversion $100\mathbf{u} - 80$ is needed to bridge the gap between the dimensionless value and the physiological unit so that $\mathbf{A}\Phi = \mathbf{B}(100\mathbf{u} - 80)$ when Φ is measured in mV. However, because a constant field has no contribution to Φ as a result of the gradient operator ∇ in $\mathbf{B}$, we have $\mathbf{A}\Phi = \mathbf{B}(100\mathbf{u} - 80) = \mathbf{B}(100\mathbf{u})$. Therefore, the implementation of TEPI does not involve any conversion of the dimensionless $\mathbf{u} \in [0, 1]$. Instead, the measured Φ (in mV) is scaled by 1/100 before being input to TEPI.

In addition to the aspects discussed above, the proposed approach of transmural EP imaging has large capacity for future developments, for example, to accommodate a wider variety of EP and imaging data, to be extended to more complex arrhythmia patterns such as VT, and to include investigations on atria.

APPENDIX

A list of the notations used in this study, including all the assumptions and parameter values used in the Bayesian estimation, is provided in Fig. 18.

ACKNOWLEDGMENT

The authors would like to thank Dr. M. Pop, Dr. G. Wright and their group (Sunnybrook Research Institute, Toronto, ON, Canada) for the acquisition and sharing of the experimental data (EP-CARTO and DW-MRI data) on the two swine models, Dr. T. Mansi (Siemens Corporate Research, Princeton, NJ, USA) for mesh generation and fiber extraction for the infarcted heart, and Dr. M. Sermesant (INRIA, Asclepios project, Sophia Antitpolis, France) for mesh generation and fiber extraction for the normal heart. The authors would like to thank Research Computing at Rochester Institute of Technology (Rochester, NY, USA) in making GPU resources available to the authors, which made the large number of experiments possible during the study.

REFERENCES

[1] W. G. Stevenson, "Ventricular scars and VT tachycardia," *Trans. Am. Clin. Climatolog. Assoc.*, vol. 120, pp. 403–412, 2009.

[2] S. Nakahara, M. Veseghi, R. J. Ramirez, C. G. Fonseca, C. K. Lai, J. P. Finn, A. Mahajan, N. G. Boyle, and K. Shivkumar, "Characterization of myocardial scars: Electrophysiological imaging correlates in a porcine infarct model," *Heart Rhythm*, vol. 8, pp. 1060–1067, 2011.

[3] T. Dickfeld, J. Tian, G. Ahmad, A. Jimenez, A. Turgeman, R. Kuk, M. Peters, A. Saliaris, M. Saba, S. Shorofsky, and J. Jeudy, "MRI-guided ventricular tachycardia ablation: Integration of late gadolinium-enhanced 3-D scar in patients with implantable cardioverter-defibrillators," *Circulat. Arrhythmia Electrophysiol.*, vol. 4, pp. 172–184, 2011.

[4] S. Nazarian, D. A. Bluemke, A. C. Lardo, M. M. Zviman, S. P. Watkins, T. L. Dickfeld, G. R. Meininger, A. Roguin, H. Calkins, G. F. Tomaselli, R. G. Weiss, R. D. Berger, J. A. C. Lima, and H. R. Halperin, "Magnetic resonance assessment of the substrate for inducible ventricular tachycardia in nonischemic cardiomyopathy," *Circulation*, vol. 112, pp. 2821–2825, 2005.

[5] A. Codreanu, F. Odille, E. Aliot, P. Marie, I. Magnin-Poull, M. Andronache, D. Mandry, W. Djaballah, D. Regent, J. Felblinger, and C. de Chillou, "Electroanatomic characterization of post-infarct scars: Comparison with 3-dimensional myocardial scar reconstruction based on magnetic resonance imaging," *J. Am. Coll. Cardiol.*, vol. 52, no. 10, pp. 839–842, 2008.

[6] A. P. Wijnmaalen, R. J. van der Geest, C. F. B. van Huls van Taxis, H. J. Siebelink, L. J. M. Kroft, J. J. Bax, J. H. C. Reiber, M. J. Schalij, and K. Zeppenfeld, "Head-to-head comparison of contrast-enhanced magnetic resonance imaging and electroanatomical voltage mapping to assess post-infarct scar characteristics in patients with ventricular tachycardias: Real-time image integration and reversed registration," *Eur. Heart J.*, vol. 32, pp. 104–114, 2011.

[7] R. Plonsey, *Bioelectric Phenomena*. New York: McGraw Hill, 1969.

[8] Y. Rudy and B. Messinger-Rapport, "The inverse problem of electrocardiography: Solutions in terms of epicardial potentials," *CRC Crit. Rev. Biomed. Eng.*, vol. 16, pp. 215–268, 1988.

[9] Y. Zhang, A. Ghodrati, and D. H. Brooks, "An analytical comparison of three spatio-temporal regularization methods for dynamic linear inverse problems in a common statistical framework," *Inverse Problems*, vol. 21, pp. 357–382, 2005.

[10] G. Huiskamp and F. Greensite, "A new method for myocardial activation imaging," *IEEE Trans. Biomed. Eng.*, vol. 44, no. 6, pp. 446–446, Jun. 1997.

[11] P. M. van Dam, T. F. Oostendorp, A. C. Linnenbank, and A. van Oosterom, "Noninvasive imaging of cardiac activation and recovery," *Ann. Biomed. Eng.*, vol. 37, no. 9, pp. 1739–1756, 2009.

[12] Z. Liu, C. Liu, and B. He, "Noninvasive reconstruction of three-dimensional ventricular activation sequence from the inverse solution of distributed equivalent current density," *IEEE Trans. Med, Imag,*, vol. 25, no. 10, pp. 1307–1318, Oct. 2006.

[13] L. Wang, H. Zhang, H. Liu, and P. Shi, "Imaging of 3-D cardiac electrical activity: A model-based recovery framework," in *Proc. Med. Image Computing Computer Assist. Intervent.*, 2006, pp. 792–799.

[14] L. Wang, H. Zhang, K. Wong, H. Liu, and P. Shi, "Physiological-model-constrained noninvasive reconstruction of volumetric myocardial transmembrane potentials," *IEEE Trans. Biomed. Eng.*, vol. 5, no. 2, pp. 296–315, Feb. 2010.

[15] V. S. Chauhan, E. Downar, K. Nanthakumar, J. D. Parker, H. J. Ross, W. Chan, and P. Picton, "Increased ventricular repolarization heterogeneity in patients with ventricular arrhythmia vulnerability and cardiomyopathy: A human in vivo study," *Am. J. Physiol. Heart Circulat. Physiol.*, vol. 290, pp. H79–H86, 2006.

[16] L. Wang, F. Dawoud, K. Wong, H. Zhang, H. Liu, J. Sapp, M. Horacek, and P. Shi, "Mapping the transmural scar and activation for patients with ventricular arrhythmia," in *Proc. IEEE Int. Conf. Comput. Cardiol.*, 2011, vol. 38, pp. 849–852.

[17] L. Wang, H. Zhang, K. Wong, H. Liu, and P. Shi, "Noninvasive computational imaging of cardiac electrophysiology for 3-D infarct," *IEEE Trans. Biomed. Eng.*, vol. 58, no. 4, pp. 1033–1043, Apr. 2011.

[18] M. Pop, M. Sermesant, T. Mansi, E. Crystal, S. Ghate, J. Relan, C. Pierre, Y. Coudiere, J. Barry, I. Lashevsky, B. Qiang, E. R. McVeigh, N. Ayache, and G. A. Wright, "Forward approaches to computational electrophysiology using MRI-based models and in-vivo CARTO mapping of swine hearts," in *Proc. Stat. Atlases Computat. Models Heart*, 2012, pp. 1–13.

[19] L. Wang, H. Zhang, K. Wong, H. Liu, and P. Shi, "Electrocardiographic simulation on personalized heart-torso structures using coupled mesh-free-BEM platform," *Int. J. Funct. Informat. Personal. Med.*, vol. 2, no. 2, pp. 175–200, 2009.

[20] D. Wang, R. M. Kirby, and C. R. Johnson, "Resolution strategies for the finite element based solution of the electrocardiographic inverse problem," *IEEE Trans. Biomed. Eng.*, vol. 57, no. 2, pp. 220–237, Feb. 2004.

[21] R. R. Aliev and A. V. Panfilov, "A simple two-variable model of cardiac excitation," *Chaos, Solitons Fractals*, vol. 7, no. 3, pp. 293–301, 1996.

[22] D. Durrer, R. T. van Dam, G. E. Freud, M. J. Janse, F. L. Meijler, and R. C. Arzbaecher, "Total excitation of the isolated human heart," *Circulation*, vol. 41, pp. 899–912, 1970.

[23] J. Butcher, *Numerical Methods for Ordinary Differential Equations*. New York: Wiley, 2008.

[24] S. Julier, "The scaled unscented transform," *Int. J. Num. Methods Eng.*, vol. 47, pp. 1445–1462, 2000.

[25] J. V. Candy, *Bayesian Signal Processing: Classical, Modern and Particle Filtering Methods*. New York: Wiley, 2008.

[26] M. Corraine, S. Lopez, and L. Wang, "Gpu acceleration of transmural electrophysiological imaging," in *Proc. IEEE Conf. Comput. Cardiol.*, 2012, pp. 849–852.

[27] M. D. Cerqueira, N. J. Weissman, V. Dilsizian, A. K. Jacobs, S. Kaul, W. K. Lasky, D. J. Pennell, J. A. Rumberger, T. Ryan, and M. S. Verani, "Standardized myocardial segmentation and nomenclature for tomographic imaging of the heart," *Circulation*, vol. 105, pp. 539–542, 2002.

[28] J. Relan, M. Pop, H. Delingette, G. A. Wright, N. Ayache, and M. Sermesant, "Personalization of a cardiac electrophysiology model using optical mapping and MRI for prediction of changes with pacing," *IEEE Trans. Biomed. Eng.*, vol. 58, no. 12, pp. 3339–3349, Dec. 2011.

[29] E. X. Wu, Y. Wu, J. M. Nicholls, J. Wang, S. Liao, S. Zhu, C. P. Lau, and H. F. Tse, "MR diffusion tensor imaging study of postinfarct myocardium structural remodeling in a porcine model," *Magn. Reson. Med.*, vol. 58, no. 4, pp. 687–695, 2007.

[30] H. Ashikaga *et al.*, "Electromechanical analysis of infarct border zone in chronic myocardial infarction," *Am. J. Physiol.-Heart Circulat. Physiol.*, vol. 289, pp. H1099–H1105, 2005.

[31] E. Konukoglu, J. Relan, U. Cilingir, B. H. Menze, P. Chinchapatnam, A. Jadidi, H. Cochet, M. Hocini, H. Delingette, P. Jais, M. Haissaguerre, N. Ayache, and M. Sermesant, "Efficient probabilistic model personalization integrating uncertainty on data and parameters: Application to eikonal-diffusion model in cardiac electrophysiology," *Progress Biophys. Molecular Biol.*, vol. 107, no. 1, pp. 134–146, 2011.

[32] C. Phillips, J. Mattout, M. D. Rugg, P. Maquet, and K. J. Friston, "An empirical Bayesian solution to the source reconstruction problem in EEG," *Neuroimage*, vol. 24, pp. 997–1011, 2005.

[33] J. Xu, A. Rahimi, F. Gao, and L. Wang, "Localization of sparse transmural excitation stimuli from surface mapping," in *Proc. Med. Image Computing Computer Assist. Intervent.*, 2012, pp. 675–682.

[34] O. Camara, M. Sermasant, P. Lamata, L. Wang, M. Pop, J. Relan, M. D. Craene, H. Delingette, H. Liu, S. Niederer, A. Pashaei, G. Plank, D. Romero, R. Sebastian, K. Wong, H. Zhang, N. Ayache, A. Frangi, P. Shi, N. P. Smith, and G. A. Wright, "Inter-model consistency and complementarity: Learning from ex-vivo imaging and electrophysiological data towards an integrated understanding of cardiac physiology," *Prog. Biophys. Molecular Biol.*, vol. 107, pp. 122–133, 2011.

[35] D. Wang, R. M. Kirby, R. S. Macleod, and C. R. Johnson, "Identifying myocardial ischemia by inversely computing transmembrane potentials from body-surface potential maps," in *Proc. Int. Symp. Noninvasive Funct. Source Imag. Brain Heart*, 2011, pp. 121–125.